IQ-Collaboratory 1.1: The Star-forming Sequence of Simulated Central Galaxies

ChangHoon Hahn[1,2], Tjitske K. Starkenburg[3] , Ena Choi[4] , Romeel Davé[5], Claire M. Dickey[6], Marla C. Geha[6] ,
Shy Genel[3,7] , Christopher C. Hayward[3] , Ariyeh H. Maller[8,9] , Nityasri Mandyam[10], Viraj Pandya[11] , Gergö Popping[12] ,
Mika Rafieferantsoa[13,14,15], Rachel S. Somerville[3,16], and Jeremy L. Tinker[10]

[1] Lawrence Berkeley National Laboratory, 1 Cyclotron Road, Berkeley, CA 94720, USA; hahn.changhoon@gmail.com
[2] Berkeley Center for Cosmological Physics, University of California, Berkeley, CA 94720, USA
[3] Flatiron Institute, 162 Fifth Avenue, New York, NY 10010, USA
[4] Department of Astronomy, Columbia University, 550 West 120th Street, New York, NY 10027, USA
[5] Institute for Astronomy, Royal Observatory, Edinburgh EH9 3HJ, UK
[6] Department of Astronomy, Yale University, New Haven, CT 06520, USA
[7] Columbia Astrophysics Laboratory, Columbia University, 550 West 120th Street, New York, NY 10027, USA
[8] Department of Physics, New York City College of Technology, CUNY, 300 Jay Street, Brooklyn, NY 11201, USA
[9] Department of Astrophysics, American Museum of Natural History, New York, NY 10024, USA
[10] Center for Cosmology and Particle Physics, Department of Physics, New York University, New York, NY 10003, USA
[11] UCO/Lick Observatory, Department of Astronomy and Astrophysics, University of California, Santa Cruz, CA 95064, USA
[12] Max-Planck-Institut für Astronomie, Königstuhl 17, D-69117 Heidelberg, Germany
[13] University of the Western Cape, Bellville, Cape Town 7535, South Africa
[14] South African Astronomical Observatory, Observatory, Cape Town 7925, South Africa
[15] Max-Planck-Institüt für Astrophysik, D-85748 Garching, Germany
[16] Department of Physics and Astronomy, Rutgers, The State University of New Jersey, 136 Frelinghuysen Road, Piscataway, NJ 08854, USA

Abstract

A tightly correlated star formation rate (SFR)–stellar mass relation of star-forming galaxies, or star-forming sequence (SFS), is a key feature in galaxy property-space that is predicted by modern galaxy formation models. We present a flexible data-driven approach for identifying this SFS over a wide range of SFRs and stellar masses using Gaussian mixture modeling (GMM). Using this method, we present a consistent comparison of the $z = 0$ SFSs of central galaxies in the Illustris, Evolution and Assembly of GaLaxies and their Environment, and MUFASA hydrodynamic simulations and the Santa Cruz semianalytic model (SC-SAM), alongside data from the Sloan Digital Sky Survey. We find, surprisingly, that the amplitude of the SFS varies by up to ~0.7 dex (factor of ~5) among the simulations with power-law slopes ranging from 0.7 to 1.2. In addition to the SFS, our GMM method also identifies subcomponents in the SFR–stellar mass plane corresponding to starburst, transitioning, and quiescent subpopulations. The hydrodynamic simulations are similarly dominated by SFS and quiescent subpopulations unlike the SC-SAM, which predicts substantial fractions of transitioning and starburst galaxies at stellar masses above and below $10^{10} M_\odot$, respectively. All of the simulations also produce an abundance of low mass quiescent central galaxies in apparent tension with observations. These results illustrate that, even among models that well reproduce many observables of the galaxy population, the $z = 0$ SFS and other subpopulations still show marked differences that can provide strong constraints on galaxy formation models.

Key words: galaxies: evolution – galaxies: halos – galaxies: star formation – galaxies: statistics – methods: statistical

1. Introduction

Large galaxy surveys of the past decade, such as the Sloan Digital Sky Survey (SDSS; York et al. 2000), have firmly established the major trends of galaxies in the local universe. Galaxies broadly fall into two populations: quiescent galaxies with little star formation that are red in color with elliptical morphologies and star-forming galaxies with significant star formation that are blue in color with disk-like morphologies (Blanton et al. 2003; Kauffmann et al. 2003; Baldry et al. 2006; Taylor et al. 2009; Moustakas et al. 2013; see Blanton & Moustakas 2009 and references therein). Star-forming galaxies, furthermore, are found to have a tight relationship between their star formation rates (SFR) and stellar masses placing them on the so-called "star-forming sequence" (hereafter, SFS; e.g., Daddi et al. 2007; Noeske et al. 2007; Salim et al. 2007, see also Figure 1).

In fact, this sequence of star-forming galaxies is found in observations well beyond the local universe out to $z > 2$ (Wang et al. 2013; Leja et al. 2015; Schreiber et al. 2015). But more than its persistence, the SFS plays a crucial role in characterizing the evolving galaxy population. Although its importance is contested (Kelson 2014; Abramson et al. 2016), the most dramatic transformations of galaxies over the past 10 Gyr can be described by the SFS. For instance, the decline in the number density of massive star-forming galaxies and the accompanying growth in number density of quiescent galaxies reflects the cessation of star formation in star-forming galaxies migrating off of the SFS (Blanton 2006; Borch et al. 2006; Bundy et al. 2006; Moustakas et al. 2013). Similarly, the cosmic decline in star formation (Hopkins & Beacom 2006; Behroozi et al. 2013b; Madau & Dickinson 2014) reflects the overall decline of star formation of the SFS (Schreiber et al. 2015).

Galaxy formation models qualitatively reproduce the SFS and similar global relations of galaxy properties at $z \sim 0$ and provide insights into the key physical processes governing those relations (e.g., Genel et al. 2014; Vogelsberger et al. 2014; Schaye et al. 2015; Somerville et al. 2015; Davé et al. 2017a;
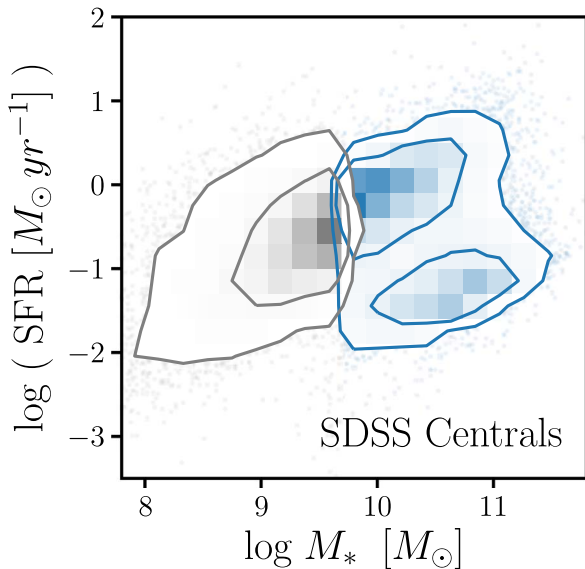
Figure 1. Star-forming central galaxies in the SDSS have a well-defined relationship between their SFRs and stellar masses, placing them on the "star-forming sequence." Our SDSS central galaxy sample is derived from a volume-limited sample from Tinker et al. (2011) at $M_* > 10^{9.7} M_\odot$ (blue) and a low luminosity sample from Geha et al. (2012) at $M_* < 10^{9.7} M_\odot$ (gray) described in Section 2.5.

flexible, data-driven method for identifying the SFS. We then use this method to compare the $z = 0$ central galaxy populations of the Illustris, Evolution and Assembly of GaLaxies and their Environment (EAGLE), and MUFASA hydrodynamic simulations and the Santa Cruz Semianalytic Model (SC-SAM), alongside observations from SDSS.

In Section 2, we describe the data sets from simulations and observations and how we specifically select our galaxy sample. Then, in Section 3, we describe how we identify the SFS with a data-driven approach using Gaussian mixture modeling. We present the resulting SFSs from the simulations and observations in Section 4 and compare the galaxy populations of the simulations and observations. Finally, we conclude and summarize the results of our comparison in Section 5. This paper is the first in a series, initialized by the IQ (Isolated & Quiescent)-Collaboratory, which aims to improve our understanding of quenching processes by comparing isolated star-forming and quiescent galaxies in simulations and observations. This first project in the IQ-Collaboratory focuses on the star-forming and quiescent galaxy populations at $z \sim 0$. Additional projects will focus on galaxy populations at $0.5 < z < 3$ during the peak of cosmic star formation (E. Choi et al. 2019, in preparation), and the gas content of star-forming and quenched galaxies (A. Emerick et al. 2019, in preparation). In the subsequent paper of this project (IQ 1.2), we will address the challenges in measured galaxy properties by forward modeling mock spectra of simulated galaxies and measuring their properties in the same manner as observations (T. K. Starkenburg et al. 2019, in preparation).

2. The Galaxy Samples

In this work, our main focus is to compare simulated central galaxies from four large-scale cosmological simulations: three hydrodynamic (Illustris, EAGLE, and MUFASA) and one semianalytic (SC-SAM). A consistent comparison requires consistently defined galaxy properties across the simulations. For all of the simulated galaxies we derive their stellar masses using the same definition and their SFRs on two timescales: instantaneous and averaged over 100 Myr. SFR on these timescales approximately correspond to $H\alpha$ and UV based SFR measurements, which represent the formation of young stars with ages $\lesssim 10$ Myr and star formation in the last ~ 100 Myr, respectively (e.g., Kennicutt & Evans 2012). We use instantaneous SFR, instead of SFR averaged over 10 Myr, to minimize resolution effects in hydrodynamic simulations on such short timescales (Appendix C).

In the hydrodynamic simulations, we derive the instantaneous SFRs from the rate of star formation in the dense and cold gas for all the gas gravitationally bound to the host halo, and the 100 Myr averaged SFRs from the ages, or formation times, of all star particles bound to the host halo (excluding stellar particles bound to subhalos). For the semianalytic model, we derive the instantaneous SFR using the Kennicutt–Schmidt relation for molecular hydrogen (based on Bigiel et al. 2008) and the derived H_2 surface density in radial bins. We derive the SC-SAM 100 Myr averaged SFRs from the total stellar mass formed in the galaxies, which is outputted from the model every 10 Myr.

For the stellar masses of all simulated galaxies, we use the total stellar mass within the host halos, discounting the stellar mass in any subhalo within the halo. Although stellar masses within some effective radius are better suited for comparison to

for a recent review, see Somerville & Davé 2015). These hydrodynamic and semianalytic simulations each seek to capture the complex physics of gas heating and cooling, star formation, stellar feedback, chemical evolution, black hole formation and evolution, and feedback from active galactic nuclei (AGNs) using their distinct subgrid model prescriptions. Many works have already compared the simulations considered in this paper to observations of, for example, galaxy masses, colors, and SFRs (e.g., Genel et al. 2014; Torrey et al. 2014; Vogelsberger et al. 2014; Schaye et al. 2015; Somerville & Davé 2015; Sparre et al. 2015; Bluck et al. 2016; Davé et al. 2017a). These works, however, primarily focus on comparing one specific simulated galaxy sample to one or a few observational data sets. Extending such comparisons to include multiple simulations, observations, and a consistent framework for comparing the data sets would allow us to make a detailed comparison of the different subgrid models and thereby provide key constraints on the physics that govern galaxy formation and evolution.

The SFS, given its prominence, naturally presents itself as a key feature in the data-space of galaxy properties to compare across both observations and simulations. Moreover, with the important role it plays in characterizing the evolving galaxy population, the SFS provides a way to interpret and understand the different galaxy subpopulations and the processes that create them. Two main challenges lie in conducting a meaningful comparison of the SFS. First is the lack of a flexible and data-driven method for identifying the SFS across different data sets. In fact, inconsistencies in how the SFS is identified have incorrectly led to agreement among simulations and observations (e.g., Somerville & Davé 2015; see Appendix A). The other challenge is the difference in methodology for deriving and tracers of galaxy properties (such as SFR, M_*), which even for the same data set dramatically impacts the SFS (e.g., Speagle et al. 2014). In this paper we address the first challenge by presenting a

Table 1

Upper Table: The Volume, Dark Matter and Baryonic Mass Resolutions (m_{DM} and m_b respectively), and Softening Lengths (ϵ) at $z = 0$ of the Illustris, EAGLE, MUFASA, and SC-SAM Simulations Described in Section 2. Bottom Table: Purity and Completeness of Central Galaxies Identified by our Group Finder, And Cosmic Star Formation Rate Densities Using Either Instantaneous and 100 Myr averaged Star Formation Rates

Simulation	Volume (Mpc^3)	m_{DM} ($10^6\,M_\odot$)	m_b ($10^6\,M_\odot$)	ϵ ($z = 0$) (kpc)
Illustris	106.5^3	6.26	1.26	0.71 (baryons); 1.42 (DM)
EAGLE	100^3	9.7	1.81	0.7
MUFASA	73.5^3	96	18.2	0.735
SC-SAM[a]	147.5^3	221	…	1.475

Simulation	Group finder purity	Group finder completeness	ρ_{SFR} (instantaneous) ($M_\odot\,yr^{-1}\,Mpc^{-3}$)	ρ_{SFR} (100 Myr) ($M_\odot\,yr^{-1}\,Mpc^{-3}$)
Illustris	99%	86%	$10^{-1.66}$	$10^{-1.68}$
EAGLE	93%	89%	$10^{-2.22}$	$10^{-2.20}$
MUFASA	84%	91%	$10^{-1.87}$	$10^{-1.91}$
SC-SAM[a]	97%	85%	$10^{-1.94}$	$10^{-1.94}$

Note.

[a] The SC-SAM is run on eight subboxes from the Bolshoi–Planck dark-matter-only N-body simulations. The dark matter particle mass and softening length quoted are for the Bolshoi–Planck simulations, and the volume quoted is for the eight combined subboxes.

observations (especially $M_* \gtrsim 10^{11}\,M_\odot$ galaxies), they are significantly impacted by the galaxy size predicted by the different subgrid models of the simulations. Since we primarily focus on comparing only simulations, we use the total stellar mass within the halo, which is easy to consistently define. Furthermore, we test using the EAGLE simulation that our analysis (i.e., the SFSs we identify) is *not* significantly impacted whether we use the total stellar masses within the halo or stellar masses within 70, 50, or 30 kpc. We reserve a more careful comparison to observations in the next paper of the series: T. K. Starkenburg et al. (2019, in preparation).

From the SFRs and stellar masses, we derive the specific-SFRs of the galaxies as $\log SSFR = \log SFR - \log M_*$. Due to the numerical and resolution effects a significant number of galaxies in the hydrodynamic simulations have 100 Myr averaged "SFR = 0," when their SFRs are below the resolution limit of the simulations. We consider these galaxies to have "unmeasurably low SFRs." For the instantaneous SFRs and both SFRs for the SC-SAM, we analogously consider $\log SFR < -4\,M_\odot\,yr^{-1}$ as "unmeasurably low SFR." We discuss in Appendix C how we treat the effect of spatial, mass, and temporal resolution of the simulations, which can impact SFR and M_*, in further detail.

In the rest of this section we provide a brief description of the Illustris, EAGLE, MUFASA, and SC-SAM simulations and each of their key subgrid and feedback prescriptions. A summary of their properties can be found in Table 1. In addition, we briefly describe the SDSS galaxy sample, which we include for reference, in Section 2.5. Lastly, we describe how we consistently identify central galaxies among the simulations and observations in Section 2.6.

2.1. Illustris

The Illustris simulation[17] (Genel et al. 2014; Vogelsberger et al. 2014; public data release Nelson et al. 2015) evolves a cosmological volume of (106 Mpc)^3 with a uniform baryonic mass resolution of $1.26 \times 10^6\,M_\odot$ using the AREPO moving-mesh code (Springel 2010). It employs subgrid models for star

formation (Springel & Hernquist 2003), Bondi-like supermassive black hole (SMBH) accretion, a phenomenological model for galactic winds (inspired by Oppenheimer & Davé 2006), and two main modes for energy injection from SMBHs (see Vogelsberger et al. 2013). When gas accretion onto the SMBH occurs at Eddington ratios >0.05, thermal energy is injected continuously in the local environment of the SMBH. At lower accretion rates, the energy injection occurs in bursts at large distances from the SMBH, generating hot bubbles in the intracluster medium (Sijacki et al. 2007). The $z = 0$ stellar mass function (SMF) and the cosmic SFR density as a function of redshift were used to tune parameters for Illustris. In addition, a parameter was introduced that controls the metallicity of the galactic winds, which was tuned to the normalization of the $z = 0$ stellar mass–gas metallicity relation of galaxies. Previous works discussing aspects of the SFS and/or quenching in Illustris include Genel et al. (2014), Vogelsberger et al. (2014), Sparre et al. (2015), Bluck et al. (2016), and Terrazas et al. (2017).

2.2. EAGLE

The Virgo Consortium's EAGLE project[18] (Crain et al. 2015; Schaye et al. 2015) is a publicly available (McAlpine et al. 2016) suite of cosmological, hydrodynamic simulations of a standard Λ cold dark matter universe. Of the simulations, we use L0100Ref, which has a volume of (100 comoving Mpc)^3 and baryonic mass resolution of $1.81 \times 10^6\,M_\odot$. It uses ANARCHY (D. Vecchia et al. 2019, in preparation; see also Appendix A of Schaye et al. 2015 and Schaller et al. 2015), which is a modified version of the *Gadget* 3 N-body/SPH code (Springel 2005) that includes modifications to the SPH formulation, time stepping, and subgrid physics. The subgrid model for feedback from massive stars and AGN is based on thermal energy injection in the interstellar matter (ISM; Dalla Vecchia & Schaye 2012). The subgrid parameters for stellar feedback and BH accretion are calibrated to reproduce the SMF and reasonable galaxy sizes at $z = 0$. The AGN feedback efficiency is constrained by the central black

hole–galaxy mass relation. The simulation resolves galaxies above $M_* > 10^8 M_\odot$. The SFR–M_* relation and quiescent fractions in EAGLE have been previously discussed in Furlong et al. (2015), Trayford et al. (2015), and the passive fraction based on mock observations in Trayford et al. (2017).

2.3. MUFASA

MUFASA is a hydrodynamic simulation with a box size of $(50 h^{-1} \text{ Mpc})^3$ and particle masses of $9.6 \times 10^7 M_\odot$ and $1.82 \times 10^7 M_\odot$ for dark matter and baryons, respectively. It uses GIZMO, a code built on GADGET that uses the Meshless Finite Mass hydrodynamics method (Hopkins 2015) rather than SPH. MUFASA includes star formation via a Kennicutt–Schmidt law based on the molecular hydrogen density as computed using the subgrid recipe in Krumholz & Gnedin (2011). It also includes two-phase kinetic outflows with scalings as predicted in the Feedback in Realistic Environments simulations (Muratov et al. 2015). Finally, it quenches massive galaxies by keeping all non-self-shielded gas within halos above a mass of $M_q > (1 + 0.48z)10^{12} M_\odot$ near the halos' virial temperature (Gabor & Davé 2015; Mitra et al. 2015). MUFASA is mainly calibrated using the SMF. The primary variable calibrated for the star formation feedback was the outflow velocity relative to the circular velocity. There was no substantial calibration of the quenching model, with the key free parameter taken directly from Mitra et al. (2015). The SMF, gas and metal content of galaxies, and color-mass diagram of MUFASA have been previously discussed in Davé et al. (2016, 2017a, 2017b).

2.4. Santa Cruz Semianalytic Model

The "Santa Cruz" SAM (SC-SAM) is a semianalytic model run on merger trees from a $(147.5 \text{ comoving Mpc})^3$ subvolume of the Bolshoi–Planck dark-matter-only N-body simulations (Rodríguez-Puebla et al. 2016). The Bolshoi–Planck simulations have particle masses of $2.21 \times 10^8 M_\odot$. The model includes schematic prescriptions for gas heating and cooling, multiphase gas partitioning, star formation, chemical evolution, feedback from stars, supernovae and SMBHs, the sizes of galactic disks and bulges, and merger-induced star-bursts and structural transformations. The SC-SAM was first presented in Somerville & Primack (1999) and Somerville et al. (2001), with significant updates described in Somerville et al. (2008a, 2008b, 2012), Porter et al. (2014), Popping et al. (2014), and Somerville et al. (2015). In this work, we use the version of the SC-SAM described in Popping et al. (2014) and Somerville et al. (2015), which includes the Gnedin & Kravtsov (2011) recipe for partitioning multiphase gas into H I, H₂, and H II based on the dark matter resolution limit, we focus our analysis on halos with $M_h > 10^{11} M_\odot$. Since this roughly corresponds to $M_* \sim 10^{8.5} M_\odot$ at $z \sim 0$, we impose a conservative cut of $M_* > 10^{8.8} M_\odot$. The SC-SAM are calibrated based on the stellar mass–halo mass relation and the SMF as well as the normalizations of the black hole mass–bulge mass relation, the stellar mass–stellar metallicity relation, and the cold gas mass–stellar mass relation. The properties of the SC-SAM galaxy population, such as the quiescent fraction have been previously discussed in Brennan et al. (2015), Somerville et al. (2015), Somerville & Davé (2015), Brennan et al. (2017), and Pandya et al. (2017).

2.5. Observed SDSS Galaxies

As a reference to our comparison of the simulated galaxies, we include SDSS galaxies from two samples: a $M_* > 10^{9.7} M_\odot$ Data Release 7 (DR7; Abazajian et al. 2009) sample and a $M_* < 10^{9.7} M_\odot$ Data Release 8 (DR8; Aihara et al. 2011) sample (blue and gray in Figure 1). At high masses, we use the volume-limited galaxy sample from Tinker et al. (2011) constructed from the NYU Value-Added Galaxy Catalog (Blanton et al. 2005). It has $M_r - 5 \log(h) < -18$ and is complete for $M_* > 10^{9.7} M_\odot$. For further details, we refer readers to Tinker et al. (2011), Wetzel et al. (2013), and Hahn et al. (2017).

At lower stellar masses, we use the isolated dwarf galaxy sample of Geha et al. (2012) from the NASA Sloan Atlas (NSA), a reprocessing of SDSS DR8. The NSA is optimized for low luminosity objects and relies on the improved background subtraction technique of Blanton et al. (2011). The catalog extends to $z \approx 0.055$ and includes recalibrated spectroscopy (Yan 2011; Yan & Blanton 2012) with much smaller errors.[19]

For both SDSS subsamples, the stellar masses are estimated using the Blanton & Roweis (2007) kcorrect code, which assumes a Chabrier (2003) IMF. The SFRs are from the current release of Brinchmann et al. (2004),[20] where they are derived using the Bruzual & Charlot (1993) model with the Charlot & Fall (2000) dust prescription and CLOUDY (version C90.04; Ferland 1996) emission line modeling. For galaxies classified as having an AGN or a composite spectrum, the SFR is measured from the D_n4000 index (Balogh et al. 1998). Additionally, for star-forming galaxies that have low S/N spectra, the SFR is derived from the Hα luminosity (Brinchmann et al. 2004). We emphasize that SSFRs $\lesssim 10^{-12} \text{ yr}^{-1}$ should only be considered upper limits to the true value (Salim et al. 2007). Given the disparate methods used for the SFR measurements, the SFRs in the SDSS sample do not entirely correspond to either the instantaneous or 100 Myr averaged SFRs of the simulations. Consequently, in this work, we compare the simulations on both timescales and refrain from detailed comparisons to SDSS.

2.6. Identifying Central Galaxies

Measurements of the quiescent fraction (e.g., Baldry et al. 2006; Peng et al. 2010; Hahn et al. 2015) and star formation quenching timescale (Wetzel et al. 2013; Hahn et al. 2017) suggest whether a galaxy is a satellite or a central galaxy influences its SFR. There may also be significant differences between the SFSs of central versus satellite galaxies (Wang et al. 2018). In this paper we focus solely on the central galaxies, which constitute the majority of massive galaxies ($M_* > 10^{9.5} M_\odot$) at $z \sim 0$.

Central classification, despite its importance, is often heterogeneously defined in the literature. Among simulations, the classification depends on the definition of halo properties, and thus on the underlying halo finders. EAGLE and Illustris use SUBFIND (Springel et al. 2001), where halos are defined as locally overdense, gravitationally bound (sub)structures within a connected region selected through a friends-of-friends (FOF; Davis et al. 1985) group finder. MUFASA and SC-SAM,

---

[19] This recalibration, however, is mostly relevant only at small equivalent width values and hence does not largely affect galaxies on the SFS.
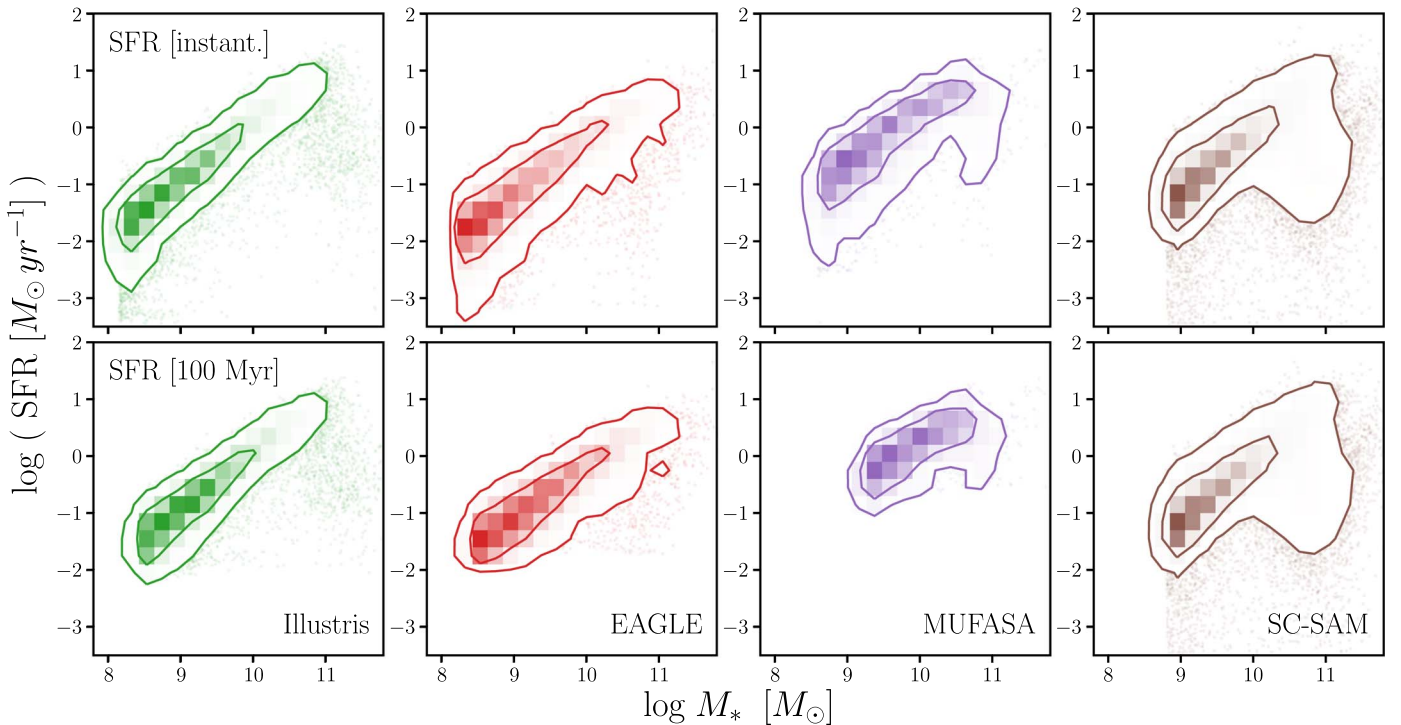[20] http://www.mpa-garching.mpg.de/SDSS/DR7/

Figure 2. SFR–M_* relations of central galaxies from the Illustris (green), EAGLE (red), and MUFASA (purple) hydrodynamic simulations and the SC-SAM (brown) at $z = 0$. The top panels use instantaneous SFRs while the bottom panels use SFRs averaged over 100 Myr. The contours in each panel mark the 68% and 95% confidence intervals of the SFR–M_* distribution. We describe the simulations and how we derive consistent SFRs and stellar masses in Section 2. The SFR–M_* relations reveal star-forming sequences in all of the simulations.

meanwhile, use ROCKSTAR (Behroozi et al. 2013a), which defines halos using a hierarchical phase-space based FOF technique and seeks to maximize the consistency of the halo through time. In addition, these central classifications also use information of the underlying dark matter—information not available in observations. Therefore, we identify central galaxies in all simulations consistently using the Tinker et al. (2011) group finder, designed to identify satellite/centrals in observations.

The Tinker et al. (2011) group finder is a halo-based algorithm that uses the abundance matching ansatz to iteratively assign halo masses to groups. It assigns a tentative halo mass to each galaxy by matching the abundance of the objects. Then starting with the most massive galaxy, nearby lower mass galaxies are assigned a probability of being a satellite. Once all the galaxies are assigned to a group, the halo masses of the central galaxies are updated by abundance matching with the total stellar mass in the groups. This entire process is repeated until convergence. In the resulting catalog, every group contains one central galaxy, which by definition is the most massive, and a group can contain zero, one, or many satellites. For a detailed description we refer readers to Tinker et al. (2011) and Wetzel et al. (2012).

Overall, we find good agreement between the central classifications of the group finder with respect to that of the simulations with purities of 99%, 93%, 84%, and 97% and completenesses of 86%, 89%, 91%, and 85% for the Illustris, EAGLE, MUFASA, and SC-SAM simulations respectively (Table 1). Differences in the purity and completeness for the simulations are likely due to the different halo finders used in the simulations. We find no significant stellar mass dependence in the purities. As expected from the high purity and completeness, when we perform our analysis using the centrals

identified by the dark matter halos, we find no significant differences. In the next section, we proceed to fitting the SFS of simulated central galaxies.

3. Identifying the SFS

We present the SFR–M_* relation of central galaxies from the observations and simulations of Section 2 in Figures 1 and 2. For both instantaneous and 100 Myr SFRs (top/bottom), in both simulations and observations, and over four orders of magnitude in SFR and stellar mass, the SFR and M_* of star-forming galaxies lie on a well-defined SFS. Despite its universality, in detail, the different data sets give rise to different SFR–M_* distributions, which makes the SFS difficult to consistently and meaningfully quantify. So far in the literature, a wide variety of fitting methods has been applied to data—even in a single comparison (see Appendix A). For example, in Lee et al. (2015) and some of the fits in Somerville & Davé (2015) the SFS is fit using median log SFRs of galaxies after some color–color or SSFR cut to the sample. Other SFSs in Somerville & Davé (2015) are fit using the median log SFRs of the entire sample. Bluck et al. (2016) fit the SFS using median log SFRs of low mass galaxies ($M_* < 10^{10} M_\odot$) and extrapolate to higher masses. Other recent works in the literature have opted for more sophisticated methods such as fitting a three-component Gaussian (Bisigello et al. 2018) or a zero-inflated negative binomial distribution (Feldmann 2017).

All of these methods require arbitrary assumptions or hard cuts to the sample. More importantly, for such methods, different assumptions or cuts produce different SFSs and inconsistent assumptions and cuts can result in misleading SFS comparisons (Appendix A). Identifying the SFS also requires

flexibility in accounting for the different features in the galaxy property space over a wide SFR or M_* range and in different simulations and observations. In an effort to better fit the SFS from a wide variety of SFR–M_* distributions and to relax the assumptions and cuts imposed on the data, we present a flexible and data-driven method for identifying the SFS that makes use of Gaussian Mixture Models.

3.1. Using Gaussian Mixture Models

Gaussian mixture models (hereafter GMM), and mixture models in general, provide a probabilistic way of describing the distribution of a population by identifying subpopulations from the data (Press et al. 1992; McLachlan & Peel 2000). Besides their extensive use in machine learning and statistics, GMMs have also been used in a wide range of astronomical analyses (e.g., Bovy et al. 2011; Lee et al. 2012; Taylor et al. 2015). Since identifying the subpopulation of star-forming galaxies from the overall galaxy population is equivalent to identifying the SFS, GMMs provides a well-motivated, data-driven, and effective method to tackle the problem.

A GMM, more precisely, is a weighted sum of k Gaussian component densities

$$\hat{p}(x; \boldsymbol{\theta}) = \sum_{i=1}^{k} \pi_i \, \mathcal{N}(x; \boldsymbol{\theta}_i), \qquad (1)$$

which can be used to estimate the density. The weights, π_i, mean, and variance $\boldsymbol{\theta}_i = \{\mu_i, \sigma_i\}$ of the components are free parameters. For a given data set $\{x_1, ..., x_n\}$, these parameters are most commonly estimated through the expectation-maximization algorithm (EM; Dempster et al. 1977; Neal & Hinton 1998).

Starting with randomly assigned $\boldsymbol{\theta}_i^0$ to the k GMM components, the EM algorithm iterates between two steps. First, for every data point, x_i, the algorithm computes for a probability of x_i being generated by each GMM component. These probabilities act as assignment weights to each of the components. Next, based on these weights, $\boldsymbol{\theta}_i^t$ of the components are updated to $\boldsymbol{\theta}_i^{t+1}$ to maximize the likelihood of the assigned data. π_i are also updated by summing up the assignment weights and normalizing the sum by the total number of data points. These steps are repeated until $p(\{x_1, ..., x_n\}; \boldsymbol{\theta}_t)$ converges. Instead of starting with randomly assigning $\boldsymbol{\theta}_i^0$, we initiate our EM algorithm using a k-means clustering algorithm (Lloyd 1982), more specifically we use the k-means++ algorithm (Arthur & Vassilvitskii 2007).

For actually identifying the SFS, we first divide the galaxy sample into stellar mass bins of some width $\Delta \log M_*$. In this paper we use bins of $\Delta \log M_* = 0.2$ dex; however, this choice does not significantly impact the final SFS. For each stellar mass bin, if there are more than $N_{\rm thresh} = 100$ galaxies in the bin, we fit the SSFR distribution using GMMs with $k = 1$ to 3 components with parameters determined from the EM algorithm described above. For the SDSS galaxy sample and all the simulations, even when we allow for more than three components, the best-fit GMMs have $k \leqslant 3$. Hence, the choice of $k \leqslant 3$ does not significantly impact the results of this work. Out of the three ($k \leqslant 3$) GMMs, we select the one with the lowest Bayesian Information Criteria (BIC; Schwarz 1978) as our "best-fit" model. BIC is often used in conjunction with GMMs (e.g., Leroux 1992; Roeder & Wasserman 1997; Fraley & Raftery 1998; Steele & Raftery 2010) and also more generally for model selection in astronomy (e.g., Liddle 2007;

Broderick et al. 2011; Vakili & Hahn 2016). In addition to the likelihood, BIC introduces a penalty term for the number of parameters in the model:

$$\mathrm{BIC} = -2 \ln \mathcal{L} + N_{\rm par} \ln N_{\rm data}. \qquad (2)$$

$N_{\rm par}$ is the total number of GMM parameters (μ_i, σ_i, and π_i) and $N_{\rm data}$ in our case is the number of galaxies in each stellar mass bin. With more components (and parameters), GMMs in principle can better fit the data; however, the BIC is lower only if the higher component GMM improves the likelihood term more than the increase in the second term of Equation (2). In this way, using BIC for our model selection not only finds a good fit to the data, but it also addresses the concern of overfitting.

Given the best-fit GMM, we next identify the SFS components in each $\log M_*$ bin. We start from the lowest $\log M_*$ bin, where we take the component with the largest weight as the SFS component. Then in the next higher $\log M_*$ bin we identify the component with the largest weight. If this component has a mean within 0.5 dex of the previous lower $\log M_*$ bin SFS component mean, we identify this component as the SFS. Otherwise, we discard it and determine whether the component with the next highest weight is within 0.5 dex of the previous SFS component mean. We repeat this until we either identify an SFS component or, if no component is within 0.5 dex of the previous SFS component mean, conclude that no SFS component is in the $\log M_*$ bin. We repeat this procedure recursively for all the $\log M_*$ bins. This scheme takes advantage of the bimodality in the SSFR distributions and has as its only assumption that the SFS forms a relatively continuous sequence. We choose 0.5 dex in order to relax any assumptions on the slope of SFS and also to avoid misclassifying the quiescent population as SFS at the high mass end. However, within the range 0.2–0.9 dex, the SFSs that we identify are not significantly impacted. In Appendix B, we present a detailed comparison of the GMM fits to the SSFR distributions of the simulations and discuss the advantages of our method in further detail.

In Figure 3, we illustrate our GMM based method for identifying the SFS of the Illustris central galaxies in two stellar mass ranges highlighted in the left panel: $10.4 < \log M_* < 10.6$ (center) and $11.0 < \log M_* < 11.2$ (right). For the two stellar mass bins, we compare the SSFR distributions of the bins to the components of the best-fit GMMs derived from our method. The SFS components of the best-fit GMMs are plotted in blue. The SSFR distribution of the center panel is best described by a GMM with three components while the SSFR distribution in the right panel is best described by a GMM with only two components. These comparisons highlight the flexibility and effectiveness of our method in identifying the SFS for different SSFR distributions. Our code for identifying the SFS makes use of the following software: *astroML* (Vanderplas et al. 2012), *astropy* (Astropy Collaboration et al. 2013; Collaboration et al. 2018), *matplotlib* (Hunter 2007), *numpy* (Van Der Walt et al. 2011), *scipy* (Jones et al. 2001), and *scikit-learn* (Pedregosa et al. 2011). The code is publicly available at https://github.com/changhoonhahn/LetsTalkAboutQuench.

4. Results

4.1. SFS of Simulated Galaxies

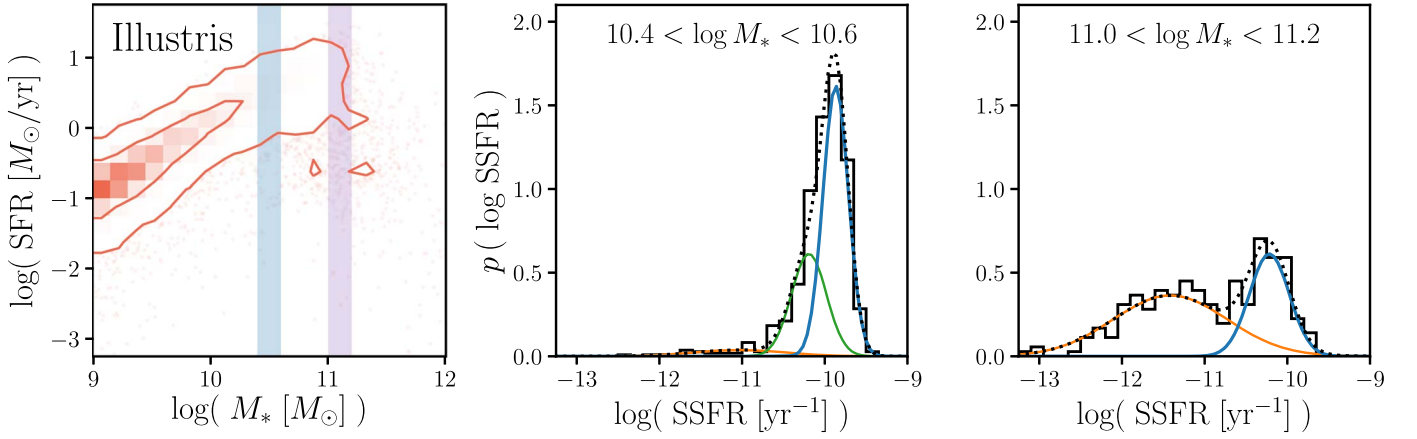Now using our GMM based method from above, we can identify the SFSs of the simulated central galaxies from

Figure 3. We illustrate our GMM based method for identifying the SFS of Illustris central galaxies in two stellar mass bins highlighted on the SFR–M_* relation of the left panel: $10.4 < \log M_* < 10.6$ and $11.0 < \log M_* < 11.2$. We compare the SSFR distributions, $p(\log \mathrm{SSFR})$, in the two stellar mass bins to their best-fit GMMs (right panels). The $p(\log \mathrm{SSFR})$ in the center panel is best described by a GMM with three components (orange, green, and blue) while the $p(\log \mathrm{SSFR})$ in the right panel is best described by a GMM with two components (orange and blue). The SFS components of the best-fit GMMs are plotted in blue. Our GMM method provides a flexible and data-driven method of identifying the SFS in a wide variety of SSFR distributions without hard assumptions or cuts to the sample.
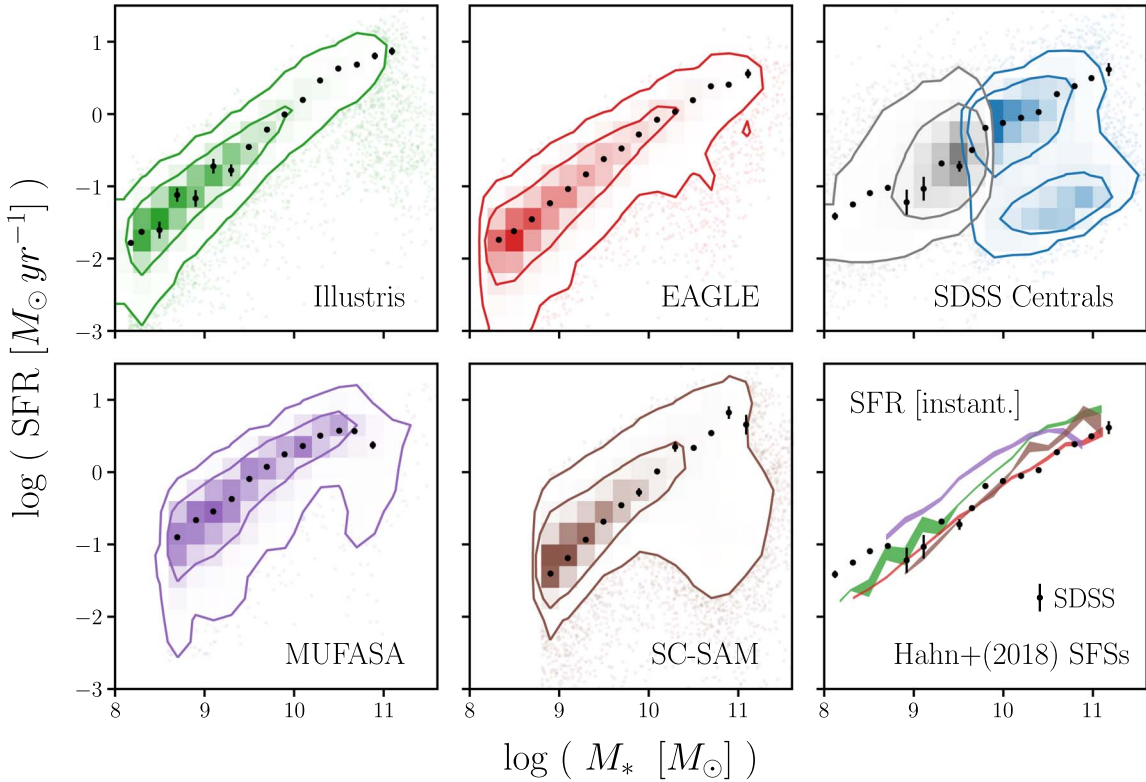
Figure 4. SFSs of the central galaxies in the Illustris, EAGLE, MUFASA, and SC-SAM simulations as identified by our GMM based method (Section 3). The SFSs above are identified from the instantaneous SFR–M_* relation. The uncertainties of the SFSs are derived using bootstrap resampling and marked by the error bars. For reference, we include the SFS of the SDSS sample in the top right panel and the bottom right panel (black). When we compare the SFSs of the simulations we find that they have significantly different slopes and their amplitudes vary by up to ∼0.7 dex, a factor of ∼5 (bottom right).

Section 2. We present the best-fit SFSs of the simulated galaxies from the Illustris, EAGLE, MUFASA, and SC-SAM simulations for the instantaneous and 100 Myr SFR timescales in Figures 4 and 5, respectively. In each simulation, for both SFR timescales, the best-fit SFS is in good agreement with the underlying SFR–M_* distribution as described by the contour and 2D histogram. However, when we compare the best-fit SFSs of the simulations to each another, we find that they have significantly different slopes and their amplitudes vary by up to ∼0.7 dex (factor of ∼5) for both the instantaneous and

100 Myr SFR timescales (bottom right panels of Figures 4 and 5).

The uncertainties for the best-fit SFSs in Figures 4 and 5 are derived from bootstrap resampling (Efron 1979) in each stellar mass bin. These uncertainties do not account for cosmic variance. Also, they correspond to the uncertainties of the means of the SFS GMM component, which is only one of the parameters in the GMM, and do not account for the correlations of other parameters of the GMM in Equation (1). Our SFS uncertainties are estimated similarly to the cluster red sequence
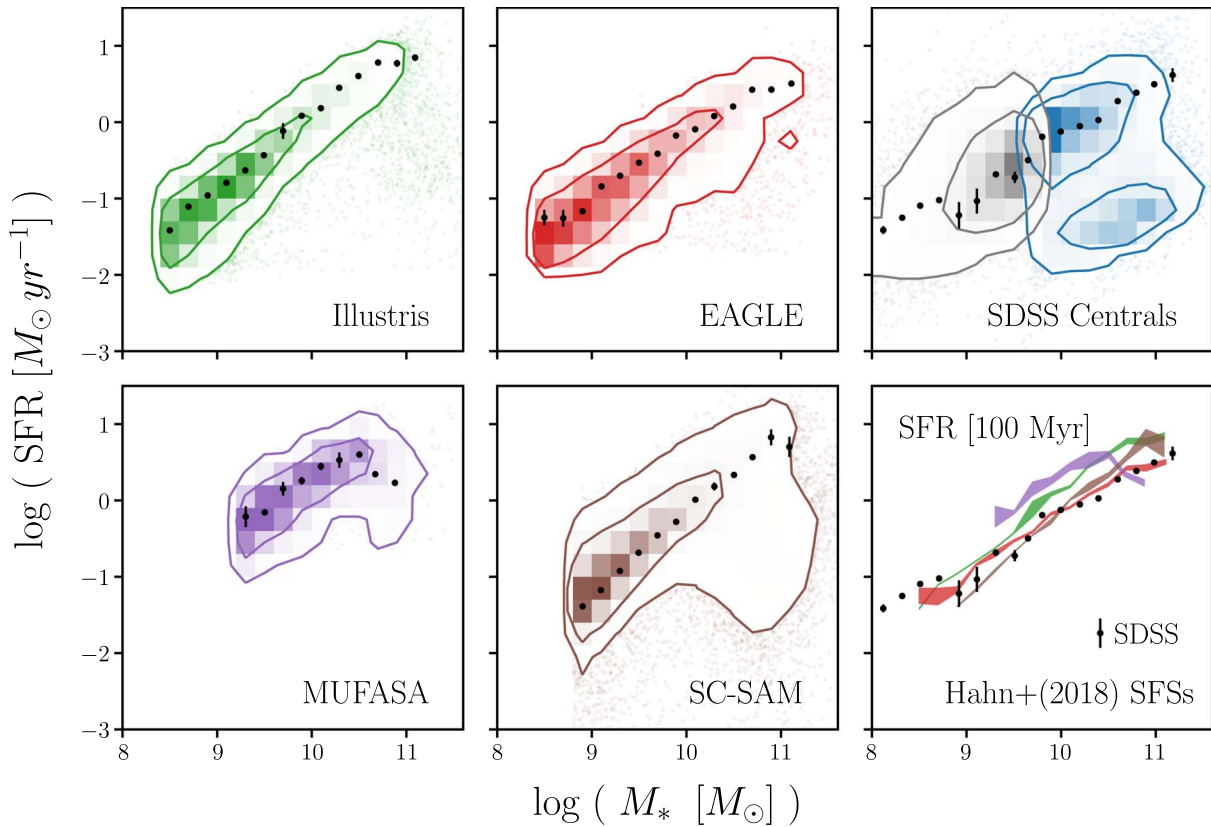
Figure 5. Same as Figure 4 but for 100 Myr SFR. As in Figure 4, the SFSs of the simulations have significantly different slopes and vary in amplitude by up to ~ 0.7 dex, a factor of ~ 5.

fits in Hao et al. (2009), which use an "error-corrected" GMM that involves bootstrap resampling. Hao et al. (2009), however, use their method to estimate the mean of their GMM component, rather than to estimate its uncertainty.

Using the SFSs we identified, we can now parameterize it to some functional form as is often done in the literature—e.g., power law (Speagle et al. 2014) or broken power law (Lee et al. 2015). With little evidence of a turnover in the SFS in most of the simulations, we fit a power law of the form

$$\log \mathrm{SFR_{MS}} = m(\log M_* - 10.5) + b \qquad (3)$$

to the SFSs in Figure 6. Unlike the SFS of other simulations, the SFSs for MUFASA have a significant turnover at $M_* \sim 10^{10.5}\, M_\odot$. This turnover is *not* caused by misidentification of the SFS or some systematic effect in the GMM fitting. Instead, the turnover is due to the halo mass dependent quenching prescription in MUFASA (Section 2.3), which causes a sharper cutoff in the SFS, unlike the other more self-consistent AGN feedback models. We focus on the power-law portion of the MUFASA SFS and fit Equation (3) below the turnover ($M_* < 10^{10.5}\, M_\odot$).

The best-fit (least squares) power-law parameters (Table 2 and Figure 6) highlight the significant differences in the slope of the SFSs. Among our simulations, m ranges from sublinear in MUFASA (0.75) to superlinear in SC-SAM (1.17). Various subgrid models (e.g., ISM, star formation, stellar and AGN feedback; see also Torrey et al. 2014) can influence the slope and normalization of SFSs in the simulations. To resolve the underlying cause behind the difference in SFSs, would require a detailed comparison of the different subgrid parameters and
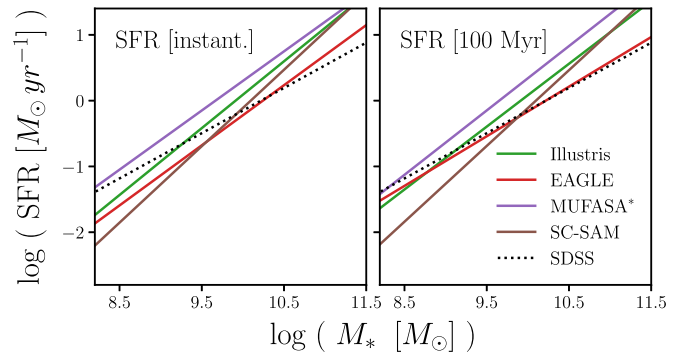

Figure 6. Power-law fits to the SFSs of the Illustris (green), EAGLE (red), MUFASA (purple), and SC-SAM (brown) simulations highlight the significant differences in the slopes of the SFSs. We use instantaneous SFR and 100 Myr SFR in the left and right panels respectively. For reference, we include the fit to the SDSS SFS (black dotted). We list the best-fit parameters in Table 2. For a consistent comparison, we fit the MUFASA SFS below $\log M_* < 10.5$, due to its high stellar mass turnover.

prescriptions. While such a comparison is beyond the scope of this paper, the discrepancies we find in the SFSs provide constraints on galaxy formation models. Furthermore, although a detailed comparison with observations is complicated by the differences in how SFR is defined in simulations versus observations, we include in Figure 6 the power-law fit to the SFS of the SDSS central galaxies (black dotted). Compared to the SFSs of the simulations, SFS in SDSS has a significantly a lower slope: $m = 0.69$. As a result, the SFSs of the simulations are scattered around the SDSS SFS below $M_* \sim 10^{10}\, M_\odot$, but have higher amplitudes than the SDSS SFS above

Table 2
Power-law Fit to the SFS of the Simulated Central Galaxies from the Illustris, EAGLE, MUFASA, and SC-SAM Simulations

Star-forming Sequence Power-law fit			Width
$\log \mathrm{SFR_{MS}} = m(\log M_* - 10.5) + b$			
Simulation	m	b	σ_{SFS} (dex)
Instantaneous SFR			
Illustris	1.01 ± 0.004	0.59 ± 0.006	0.20
EAGLE	0.91 ± 0.006	0.23 ± 0.008	0.26
MUFASA	0.75 ± 0.014	0.58 ± 0.011	0.25
MUFASA[a]	0.89 ± 0.020	0.74 ± 0.020	
SC-SAM	1.17 ± 0.008	0.48 ± 0.009	0.24
100 Myr SFR			
Illustris	0.95 ± 0.006	0.55 ± 0.008	0.18
EAGLE	0.75 ± 0.010	0.21 ± 0.009	0.20
MUFASA	0.38 ± 0.023	0.36 ± 0.016	0.25
MUFASA[a]	0.97 ± 0.050	0.83 ± 0.039	
SC-SAM	1.16 ± 0.008	0.47 ± 0.009	0.23
SDSS	0.69 ± 0.008	0.18 ± 0.007	

Note.
[a] Power-law fit to the MUFASA SFS below its turnover ($\log M_* < 10.5$).

$M_* \sim 10^{10}\,M_\odot$. This is also apparent in the bottom right panel comparisons of Figures 4 and 5.

The differences we find among the SFSs of the simulations, also appear in their cosmic star formation densities. Cosmic star formation density roughly corresponds to the total star formation in the SFS weighted by the SMF. For Illustris, EAGLE, MUFASA, and SC-SAM, respectively, we find total cosmic star formation densities (including satellites) of $10^{-1.66}$, $10^{-2.22}$, $10^{-1.87}$, and $10^{-1.94}\,M_\odot\,\mathrm{yr}^{-1}\,\mathrm{Mpc}^{-3}$ using instantaneous SFRs and similarly $10^{-1.68}$, $10^{-2.20}$, $10^{-1.91}$, and $10^{-1.94}\,M_\odot\,\mathrm{yr}^{-1}\,\mathrm{Mpc}^{-3}$ using 100 Myr SFRs (Table 1). The rank order of the densities is different than those of the SFSs due to differences in the SMFs. Although these values are roughly within the uncertainties of observations (Madau & Dickinson 2014), the difference in the star formation density between Illustris and EAGLE, for example, is greater than 0.5 dex—more than a factor of 3. With the differences among the simulations in both their cosmic star formation densities and SMFs, it is difficult to attribute the difference of the SFSs to either stellar mass or SFR alone. Differences in both properties, and therefore the full star formation history as modeled by different subgrid prescriptions in the four simulations, likely contribute to the discrepancies in the cosmic SFR densities, the SMFs, and the SFSs.

In addition to its position, μ_{SFS}, the SFS GMM component is also described by σ_{SFS}—the width of the SFS. Using σ_{SFS} derived from the GMM fitting, we can compare the width of the SFS among the simulations (Figure 7). The uncertainties for the widths are calculated through bootstrap resampling in the same way as the SFS uncertainties. Overall, we find little stellar mass dependence in σ_{SFS} for the simulations. For Illustris, EAGLE, MUFASA, and SC-SAM we, respectively, find $\sigma_{\mathrm{SFS}} \sim 0.20, 0.26, 0.25$, and 0.24 dex for instantaneous SFR and $\sigma_{\mathrm{SFS}} \sim 0.18, 0.20, 0.25$, and 0.23 dex for 100 Myr SFR (Table 2). Although we do not explicitly include the width of the SDSS SFS GMM component due to inconsistencies in the SFRs (Section 2.5), these σ_{SFS} are narrower than the ~0.3 dex width measured in observations (e.g., Daddi et al. 2007;
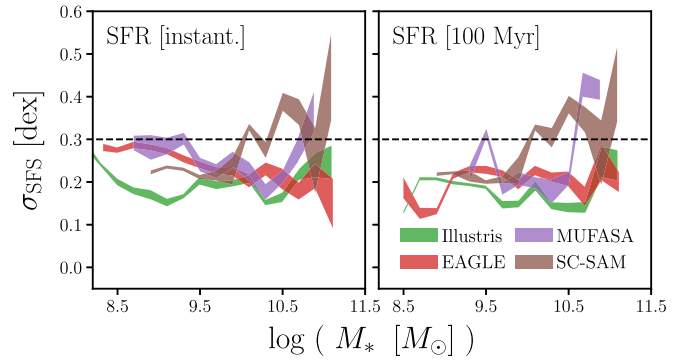

Figure 7. Width of the SFS, σ_{SFS}, for the simulated central galaxies from Illustris, EAGLE, MUFASA, and SC-SAM (green, red, purple, and brown respectively). The uncertainties are estimated using bootstrap resampling in the same way as the SFS uncertainties. The SFS widths in the simulations have little stellar mass dependence and, adding observational measurement errors in SFR, they are roughly consistent with ~0.3 dex from observations (black dashed line).

Noeske et al. 2007; Salim et al. 2007; Magdis et al. 2012; Whitaker et al. 2012; Speagle et al. 2014). Observational errors, however, will bring the simulated values to closer agreement. For instance, the SFRs of our SDSS galaxies from the NYU-VAGC have measurement errors of $\sigma_{\log \mathrm{SFR}} \approx 0.031$ dex, approximated from repeated SFR measurements of the same galaxies. Furthermore, the hydrodynamic simulations lack burstiness caused by clustered star formation, and thus feedback due to resolution effects. Sparre & Springel (2017) found that burstiness can increase $\sigma_{\log \mathrm{SFS}}$ by 0.10–0.17 dex. Additionally, Genel et al. (2018) recently showed that chaotic effects can contribute to the overall scatter in the SFS. However, because we derive σ_{SFS} from a large galaxy population this butterfly effect does not impact the measurement reliability of statistical properties of the ensemble of galaxies because the sensitivity of individual galaxy SFRs averages out. However, the different degree of the butterfly effect on different simulations may contribute the difference in σ_{SFS} among the simulations. This unresolved variability will also bring the scatter closer to the observed width. We therefore conclude that the width of the SFS from the simulations are in reasonable agreement with the observed SFS width.

Another factor that impacts the SFS we identify is the strict lower limit of the log SFRs caused by the resolution effects in the simulations. This is particularly evident in the 100 Myr SFR–M_* relations of the hydrodynamic simulations of Figure 2 —especially MUFASA. As we describe in Section 2, the 100 Myr SFRs are calculated using the ages of all star particles in a galaxy. For a galaxy to have star formation (i.e., SFR > 0), it must at least form one star particle over the last 100 Myr. A single star particle forming over 100 Myr amounts to an SFR of $\sim0.02\,M_\odot\,\mathrm{yr}^{-1}$ for Illustris and EAGLE and $\sim0.2\,M_\odot\,\mathrm{yr}^{-1}$ for MUFASA. This resolution limit, ultimately impacts the SFS at $M_* < 10^{8.4}$, $10^{8.4}$, and $10^{9.2}\,M_\odot$ for Illustris, EAGLE, and MUFASA respectively (see Appendix C).

Using our method for identifying the SFS, we are able to conduct a consistent data-driven comparison of the SFSs of simulated central galaxies from the Illustris, EAGLE, MUFASA, and SC-SAM. From this comparison, we find that the amplitudes of the SFSs differ from one another by up to ~0.7 dex, factor of ~5, with significantly different slopes. Furthermore, despite these differences, the SFSs of the simulations have similar widths, consistent with observations.
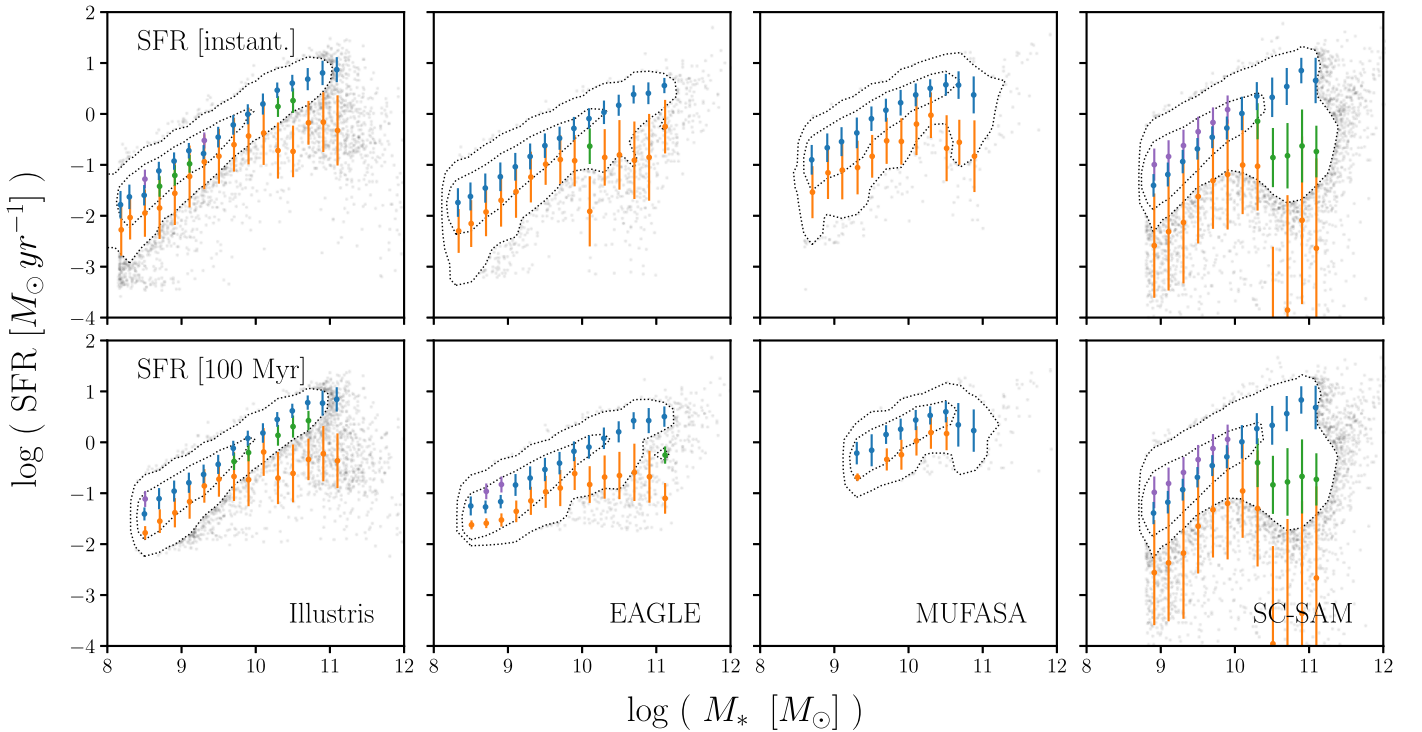
Hahn et al.

Figure 8. Components of the best-fit GMM for the SFR–M_* relations of central galaxies in the Illustris, EAGLE, MUFASA, and SC-SAM simulations (left to right). The top and bottom panels use instantaneous SFRs and 100 Myr SFRs respectively. In each $\log M_*$ bin, we mark the SFS component in blue, the low SF component in orange, the intermediate SF component in green, and the component above the SFS in purple. These components loosely correspond to the star-forming, quiescent, transitioning, and starburst subpopulations. The hydrodynamic simulations have similar subpopulations dominated by the SFS and low SF components. Meanwhile, in the SC-SAM, the GMM components reveal broad low SF components that extend out to SFR $< 10^{-4}\,M_\odot\,\mathrm{yr}^{-1}$, prominent intermediate components at $M_* \gtrsim 10^{10}\,M_\odot$, and components above the SFS at $M_* \lesssim 10^{10}\,M_\odot$.

4.2. Beyond the SFS of Simulated Galaxies

So far we have focused solely on the SFSs of the simulated galaxies—i.e., $\theta_{\mathrm{SFS}} = \{\mu_{\mathrm{SFS}}, \sigma_{\mathrm{SFS}}\}$ in Equation (1). Our GMM method, however, also determines θ_i of components other than the SFS. These GMM components provide extra features to compare the simulated galaxy samples and also offer interesting insights into the different subpopulations in the simulated galaxy samples. When we examine θ_i of all components from our fitting for the simulated galaxies, we find they loosely correspond to galaxy subpopulations typically referred to as quiescent, transitioning, and starburst (Figure 8). From the data alone, we cannot determine whether the components we identify are actually the "true" subpopulations. Therefore, to avoid overinterpreting this correspondence, we refer to the GMM component with the lowest SFR as the "low SF" component, the component with SFR in between the SFS and the low SF component as the "intermediate SF" component, and finally the component with higher SFR than the SFS component as the "high SF" component. At a given stellar mass bin, our GMM fits are restricted to $k \leqslant 3$; hence, the four different components come from different stellar mass bins. In Figure 8, we mark the SFS, low SF, intermediate SF, and high SF in blue, orange, green, and purple respectively.

Examining the GMM components of the hydrodynamic simulations in Figure 8, we find that a few $\log M_*$ bins have intermediate SF components in Illustris at $10^9\,M_\odot < M_* < 10^{11}\,M_\odot$. Also a few of the lowest $\log M_*$ bins in Illustris and EAGLE have high SF components for the 100 Myr SFRs. Besides these few bins, however, the central galaxies from the hydrodynamic simulations are dominated by the SFS and low

SF components. Furthermore, throughout the stellar mass ranges of the simulations, the low SF components in each of these simulations have relatively constant widths and lie ~1 dex below the SFS components.

Unlike the hydrodynamic simulations, however, the low SF components in the SC-SAM span out to $\log \mathrm{SFR} = -4\,M_\odot\,\mathrm{yr}^{-1}$. Furthermore, the intermediate and high SF components are much more prominent in the SC-SAM centrals. At low stellar masses ($M_* \lesssim 10^{10}\,M_\odot$) every $\log M_*$ bin has a high SF component. The $\log$ SSFR distributions in these bins have extended tails on the higher SFR side of the SFS. Our GMM method, thus, fits high SF components in these $\log M_*$ bins (bottom left and center panels of Figures 11 and 12). These high SF components and the extended range of low SF components are likely caused by the reaccretion prescription of the SAM (Section 2.7 of Somerville et al. 2008b). A fraction of gas ejected from halos (e.g., from supernovae) is kept in a reservoir, which recollapses into the halos at a later time and becomes available again for cooling. The rate of this reaccretion depends on the mass of ejected gas, the dynamical time of the halo, and a free parameter degenerate with supernovae feedback parameters. This prescription results in bursty star formation in the SC-SAM galaxies and causes the extended low SF components and the high SF components.

At high stellar masses ($M_* \gtrsim 10^{10}\,M_\odot$) every $\log M_*$ bin in the SC-SAM has an intermediate component. While the $\log$ SSFR distributions in the bottom right panels of Figures 11 and 12 and the BIC values illustrate the benefit of the GMM with an intermediate SF component, these are accentuated by the broader distribution of the low SF
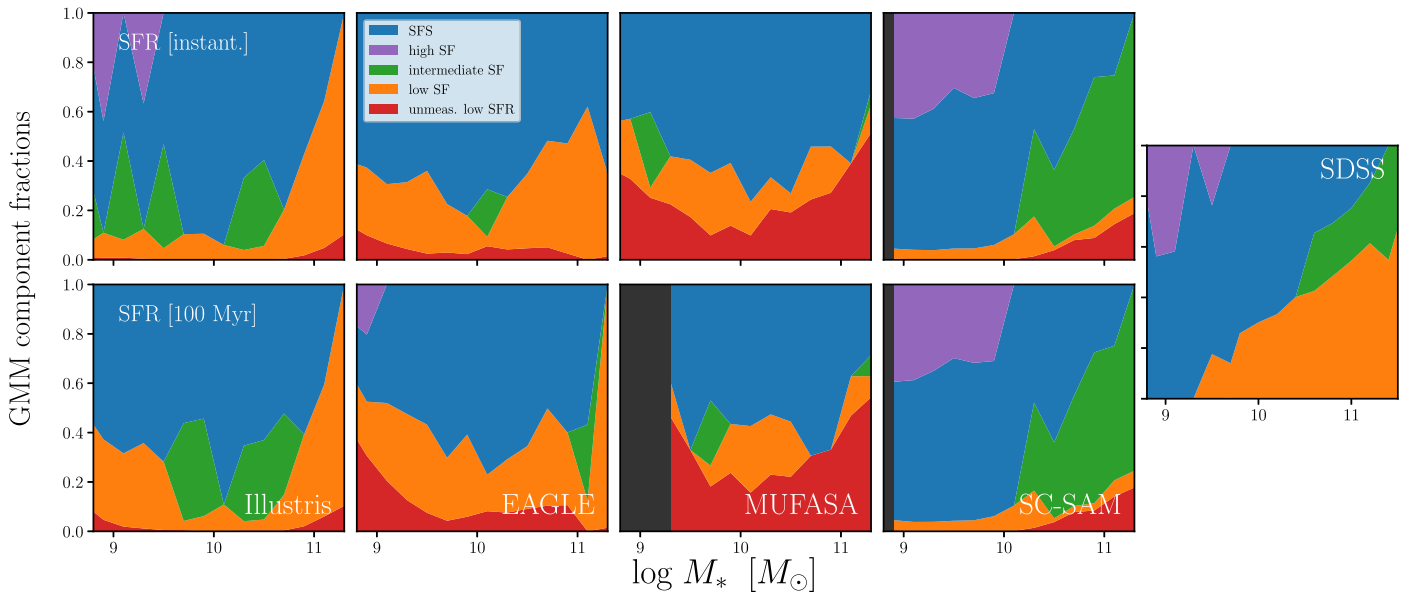
Figure 9. Fractional contributions, π_i, of the best-fit GMM components of the central galaxies in Illustris, EAGLE, MUFASA, and SC-SAM (left to right). We highlight the SFS component in blue, the low SF component in orange, galaxies with unmeasurably low SFR in red, the intermediate SF components in green, and the high SF components in purple. We shade the regions below the stellar mass limit set by resolution effects in black (Appendix C). For reference, we include π_i of the observed SDSS centrals in the rightmost panel. Unlike SDSS or the SC-SAM, we do not find significantly high SF components at low M_* in the hydrodynamic simulations. Furthermore, treating the components below the SFS as quiescent, we find little M_* dependence in the quiescent fraction at $M_* < 10^{11}\, M_\odot$ unlike observations. In fact, in all of the simulations, we find a significant fraction of quiescent central galaxies at $M_* \lesssim 10^9\, M_\odot$ contrary to observations.

population. Despite these differences between the hydrodynamic simulations and the SC-SAM, all of the simulations have a low SF component throughout their stellar mass range, even at $M_* < 10^9\, M_\odot$. We discuss these low M_* low SF galaxies in further detail later in this section.

Another set of parameters we infer from our GMM fitting is the weight of the GMM components: π_i in Equation (1). These weights correspond to the fractional contribution of the different subpopulations. For example, the weight of the low SF component loosely corresponds to the quiescent fraction (e.g., Borch et al. 2006; Bundy et al. 2006; Iovino et al. 2010; Geha et al. 2012; Hahn et al. 2015). In Figure 9, we present the fractional contribution of the components from our best-fit GMM, as a function of stellar mass: SFS (blue), low SF (orange), intermediate SF (green), and high SF (purple). We also include the fractional contribution of galaxies with unmeasurably low SFRs (red; see Section 2). The π_i have uncertainties, estimated from bootstrap resampling, on the order of $\sim$0.1.

For every simulation, a significant fraction of galaxies have unmeasurably low SFRs. In hydrodynamic simulations, a galaxy with unmeasurably low SFR can have an SFR below the resolution limit, or have a "true" SFR = 0 on the measured timescales (Appendix C). For the SC-SAM, we consider the SFR unmeasurably low when log SFR $< -4\, M_\odot\, yr^{-1}$. Therefore, in both hydrodynamic simulations and the SAM, galaxies with unmeasurably low SFR can be considered quiescent. Moreover, we confirm that SFR resolution does not significantly impact the fraction contributions of Figure 9 (see Appendix C and Figure 15).

The fractional contributions of the GMM components in Figure 9 reveal significant disagreements between the simulated galaxies and trends established from observations—especially the hydrodynamic simulations. For instance, in the hydrodynamic simulations we do not find significant high SF components at low M_*, unlike in SDSS or SC-SAM. The few

M_* bins with fractional contributions from high SF components have large bootstrap uncertainties ($\sim$0.2). Furthermore, if we treat the components below the SFS as quiescent (green, orange, and red in Figure 9), we find little stellar mass dependence in the quiescent fraction of the hydrodynamic simulations, unlike the quiescent fraction measurements of isolated SDSS galaxies (Baldry et al. 2006; Peng et al. 2010; Hahn et al. 2015). Meanwhile, at $M_* > 10^9\, M_\odot$ the SC-SAM is roughly consistent with SDSS (rightmost panel) and in agreement with previous SC-SAM quiescent fraction comparisons to observations (Brennan et al. 2015, 2017; Pandya et al. 2017).

Furthermore, for some of the hydrodynamic simulations in Figure 9 (Illustris, EAGLE, and MUFASA with 100 Myr SFRs and EAGLE, and MUFASA instantaneous SFRs) we find surprisingly high quiescent fractions ($\sim$0.4) at low masses in stark contrast with observations (Baldry et al. 2006; Peng et al. 2010; Hahn et al. 2015). In fact, all the simulations, even the SC-SAM, have nonnegligible ($\gtrsim$10%) quiescent fractions at $M_* < 10^9\, M_\odot$ contrary to the M_* lower bound of $\sim$$10^9\, M_\odot$ for isolated/central quiescent galaxies we observe in SDSS and established in the literature (e.g., Geha et al. 2012).

One possible explanation for the significant fraction of low SF galaxies at low M_* in the hydrodynamic simulations is misclassification of "splashback" (or "blacksplash" or "ejected") galaxies as centrals. Splashback galaxies are satellite galaxies that have orbited outside the virial radii of its host halo after having passed through it (e.g., Mamon et al. 2004; Gill et al. 2005; Wang et al. 2009; Wetzel et al. 2014). The SC-SAM is not subject to this misclassification because subhalos are not tracked after first infall, so by construction the model does not have splashbacks. To test whether splashbacks impact our results for the hydrodynamic simulations, we adjust our central galaxy selection criteria in Section 2.6 to exclude any centrals within three virial radii of a more massive halo. When we use this stricter central classification and measure the SFS

and other GMM components, we find no significant change to the SFS fits or the fractional contributions of the GMM components. We also find no significant changes to our results when we restrict the selection to galaxies with no "luminous" neighbors within $1.5\,\mathrm{Mpc}\,h^{-1}$—analogous to the Geha et al. (2012) criteria. We therefore conclude that the significant fraction of low SFR and low M_* galaxies is not caused by misclassification of centrals.

Another possible explanation for the abundance of low SFR galaxies at low M_*, is that the hydrodynamic simulations have insufficient resolution for galaxies with $M_* < 10^9\,M_\odot$. Low M_* galaxies in reality may have star-forming clumps with masses lower than the baryonic particle mass. Such star formation will not be captured by the simulations (Sparre & Springel 2017). We test whether our results are impacted by the resolution limit using a higher resolution box ($8\times$ higher baryon mass resolution) for EAGLE. Although the fractional contributions of the low SFR GMM component is significantly lower at $M_* \sim 10^{10}\,M_\odot$, this can also be affected by the low number of galaxies in this mass range in the small high resolution box. We still find an abundance of low SFR galaxies at $M_* < 10^9\,M_\odot$ for the higher resolution EAGLE simulation, but as the fraction increases toward lower masses we cannot rule out resolution as the cause of the low mass, low SFR component.

Taking a step back, we emphasize that this discrepancy between the simulations and observations must be taken with a grain of salt and our comparison is not an apples-to-apples comparison. For instance, in Geha et al. (2012) low SF/quiescent galaxies are classified based on a Hα emission and D_n4000 criteria—different than in the simulations. Even the central (isolation in Geha et al. 2012) criteria, in detail, is different than the analogous criteria above. More broadly, the comparisons we present in this paper are among simulations and therefore are based on "theoretical" predictions of galaxy properties. Many factors make it difficult to robustly extend this comparison to observations.

For example, SFR and M_*, the galaxy properties considered in this paper, in simulations can be directly measured either using star or gas particles in the simulations. In observations, even the SFR alone is estimated from SFR indicators such as Hα flux, D_n4000, or UV brightness and dust absorption measurements. While they serve as estimates of the SFRs, as Speagle et al. (2014) find, even for the same SDSS galaxies, different SFR indicators can produce large discrepancies in the slope and amplitude of the SFS. For M_*, because we include all stellar particles to compute the stellar masses in the simulations, this may overestimate M_*, in particular, for high mass galaxies. However, as we mention in Section 2, for the EAGLE sample, the SFS we identify does not change when we use stellar mass and SFR in the entire subhalo or within apertures of 70, 50, or 30 kpc. Furthermore, a consistent comparison to observations requires a thorough understanding of the selection effects that come with the observed galaxy sample. These effects are difficult to propagate into SFR and M_* space of simulations.

Therefore, while we note some of the differences in Figures 4–6 and 9, between the simulations and observations, we reserve a more detailed comparison to the next paper in our series: T. K. Starkenburg et al. (2019, in preparation). In this next paper, instead of comparing the "theoretical" galaxy properties, we forward model galaxy spectra and photometry of simulated galaxies using their star formation histories, make observationally motivated measurements of SFR and M_* on the synthetic spectra and photometry, and conduct a quantitative, apples-to-apples, comparison of the simulations to observations.

In this section, we demonstrate that our method for identifying the SFS provides additional features besides the SFSs, to compare different galaxy samples. These extra components offer insights into the distinct galaxy subpopulations of the simulations. Based on the non-SFS components/populations, we find that the hydrodynamic simulations are similarly dominated by the SFS and low SF components, while the SC-SAM predicts substantial fractions of high and intermediate SF components. Moreover, we find that all of the simulations have a significant fraction of low SFR central galaxies at $M_* \lesssim 10^9\,M_\odot$, contrary to observations. Furthermore, the hydrodynamic simulations, at even $M_* \lesssim 10^{11}\,M_\odot$, do not reproduce the quiescent fractions from the literature or their stellar mass dependence.

5. Summary and Conclusions

The SFS provides a key feature in galaxy property space to consistently compare galaxy populations in simulations and observations. Such comparisons are crucial for validating our theories of galaxy formation and evolution. However, they face two main challenges: the lack of a consistent data-driven method for identifying the SFS and the discrepancies in methodology for deriving galaxy properties such as SFR and M_*. In this paper, we address the former by presenting a flexible data-driven method for identifying the SFS.

Our method takes advantage of Gaussian mixture models to fit the SFR distributions in stellar mass bins and BIC for model selection. This data-driven approach allows us to robustly fit the SFR–M_* relation of galaxy populations and identify the SFS, while relaxing many of the assumptions and hard cuts that go into other methods. Furthermore, it allows us to identify the SFS over a wide range of star formation and stellar masses down to $M_* \sim 10^8\,M_\odot$. Finally, our method also allows us to identify subpopulations of galaxies, beyond the SFS, that correspond to the quiescent, transitioning, and starburst galaxy populations.

Next we apply our method to the central galaxies of the Illustris, EAGLE, and MUFASA hydrodynamic simulations and the SC-SAM. The central galaxies are identified in the simulations using the Tinker et al. (2011) group finder and have consistently derived M_* and SFRs on instantaneous and 100 Myr timescales. For reference, we also apply our method to central galaxies from SDSS observations. Comparing the resulting SFSs and other components from the simulations and observations, we find the following:

1. The identified SFSs of Illustris, EAGLE, MUFASA, and SC-SAM vary by up to $\sim$0.7 dex (a factor of $\sim$5) and have significantly different slopes over the stellar mass range $10^{8.5}\,M_\odot < M_* < 10^{11}\,M_\odot$ with little mass dependence on the discrepancies. Meanwhile, the width of the SFSs are consistent with one another and in agreement with the $\sim$0.3 dex width from observations.

2. From the best-fit GMMs, we find that the hydrodynamic simulations are mainly dominated by the SFS and low SF (quiescent) components. Meanwhile, the SC-SAM is composed of a substantial fraction of galaxies between
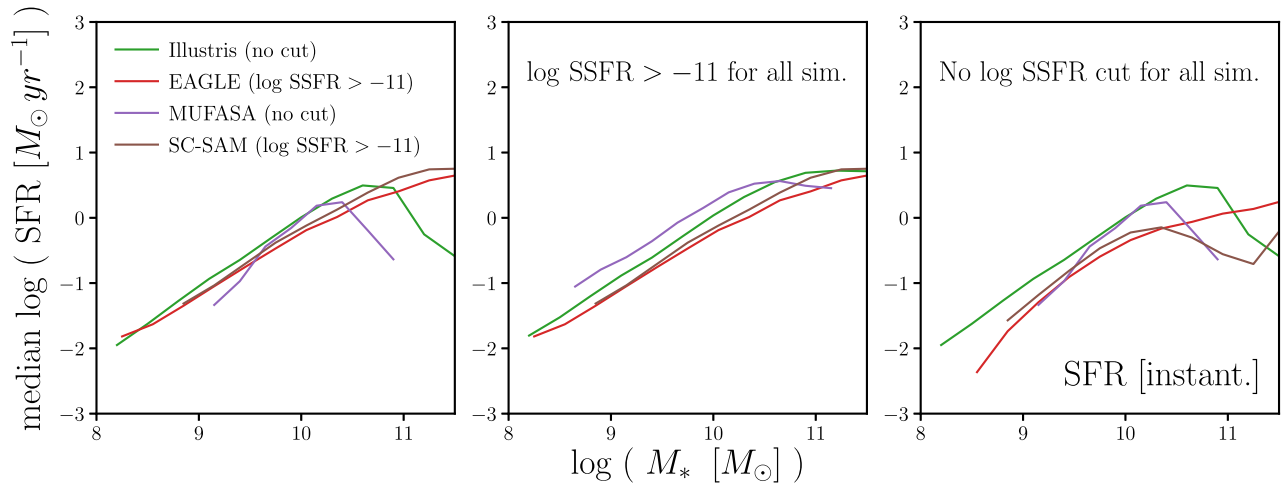
Figure 10. The SFSs of Illustris, EAGLE, MUFASA, and SC-SAM central galaxies, where we measure the SFSs using different methods as in Figure 5 of Somerville & Davé (2015; left panel) and using the same methods (center and right panels). In the left panel, we measure the SFSs by taking the median SFR in an M_* bin with no selection cuts for Illustris and MUFASA and by taking the median SFR after an SSFR $> 10^{-11}$ yr^{-1} cut for EAGLE and SC-SAM. In the center panel, we measure the SFSs by taking the median SFR after an SSFR $> 10^{-11}$ yr^{-1} cut for all four simulations. In the right panel, we measure the SFSs by taking the median SFR with no selection cuts for all four simulations. The difference among the panels illustrates that the agreement found in the left panel, and similarly in Somerville & Davé (2015), is mainly driven by the difference in methods used to measure SFSs.

the SFS and low SF components at high masses ($M_* > 10^{10}\, M_\odot$) and above the SFS at low masses ($M_* < 10^{10}\, M_\odot$), likely due to its reaccretion prescription.

3. The quiescent fractions of the hydrodynamic simulations, estimated from the components of the best-fit GMMs below the SFS and galaxies with unmeasurably low SFR, have little stellar mass dependence and are inconsistent with the SC-SAM as well as with observations. Moreover, in all of the simulations, we find an abundance of low mass ($M_* < 10^9\, M_\odot$) quiescent central galaxies, which we do not find in SDSS or the literature.

With a consistent treatment of the simulations and our method for identifying their SFSs and other subpopulations, we demonstrate significant differences in the central galaxy populations of Illustris, EAGLE, MUFASA, and SC-SAM. Although we refrain from a detailed comparison with observations, we also find significant differences between the simulations and established trends in observations. These discrepancies, which previous comparisons failed to identify, underscore the importance of a consistent data-driven approach for accurately comparing galaxy populations.

Furthermore these results illustrate how differences in the subgrid physics of the simulations propagate into significant differences in the properties of their galaxy populations. Extending our approach of a consistent data-driven comparison, to observations, we can test the subgrid physics of simulations and derive strong constraints on our galaxy formation models. This is exactly what we will present in the subsequent paper of our series —T. K. Starkenburg et al. (2019, in preparation).

Appendix A
Previous Comparisons of the SFS

Earlier SFS comparisons in the literature, overall, report agreement among simulations and observations at $z = 0$ (e.g., Genel et al. 2014; Schaye et al. 2015; Somerville & Davé 2015; Sparre et al. 2015; Bluck et al. 2016; Davé et al. 2016). This agreement is particularly evident in the comparison in Somerville & Davé (2015; Figure 5). However, as Somerville & Davé (2015) note, the SFSs compiled in the comparison are derived inconsistently, with some applying a star-forming galaxy selection cut (e.g., SSFR cut) and others not applying any cut. We demonstrate in this section that inconsistency in measuring the SFS can produce misleading agreement among simulations.

In the left panel of Figure 10 we reproduce the SFS comparison of Somerville & Davé (2015) Figure 5 for the simulations in Section 2 using different methods for measuring the SFS. For Illustris and EAGLE, we apply the same methods as the SFSs in Somerville & Davé (2015): the median SFR in a M_* bin with no selection cut for Illustris (green) and with an SSFR $> 10^{-11}$ yr^{-1} cut for EAGLE (red; Schaye et al. 2015). MUFASA and the current version of SC-SAM did not exist and were not included in Somerville & Davé (2015). Since we are illustrating how inconsistent SFS measurements can result in misleading agreement, for MUFASA and SC-SAM we measure the median SFR with no selection cut and with an SSFR $> 10^{-11}$ yr^{-1} cut, respectively. As in Figure 5 of Somerville & Davé (2015), we find good agreement among the SFSs of the simulations.

Instead of measuring the SFSs differently, if we measure the SFS by taking the median SFR after either an SSFR $> 10^{-11}$ yr^{-1} cut or with no SSFR cut consistently for all the simulations, we
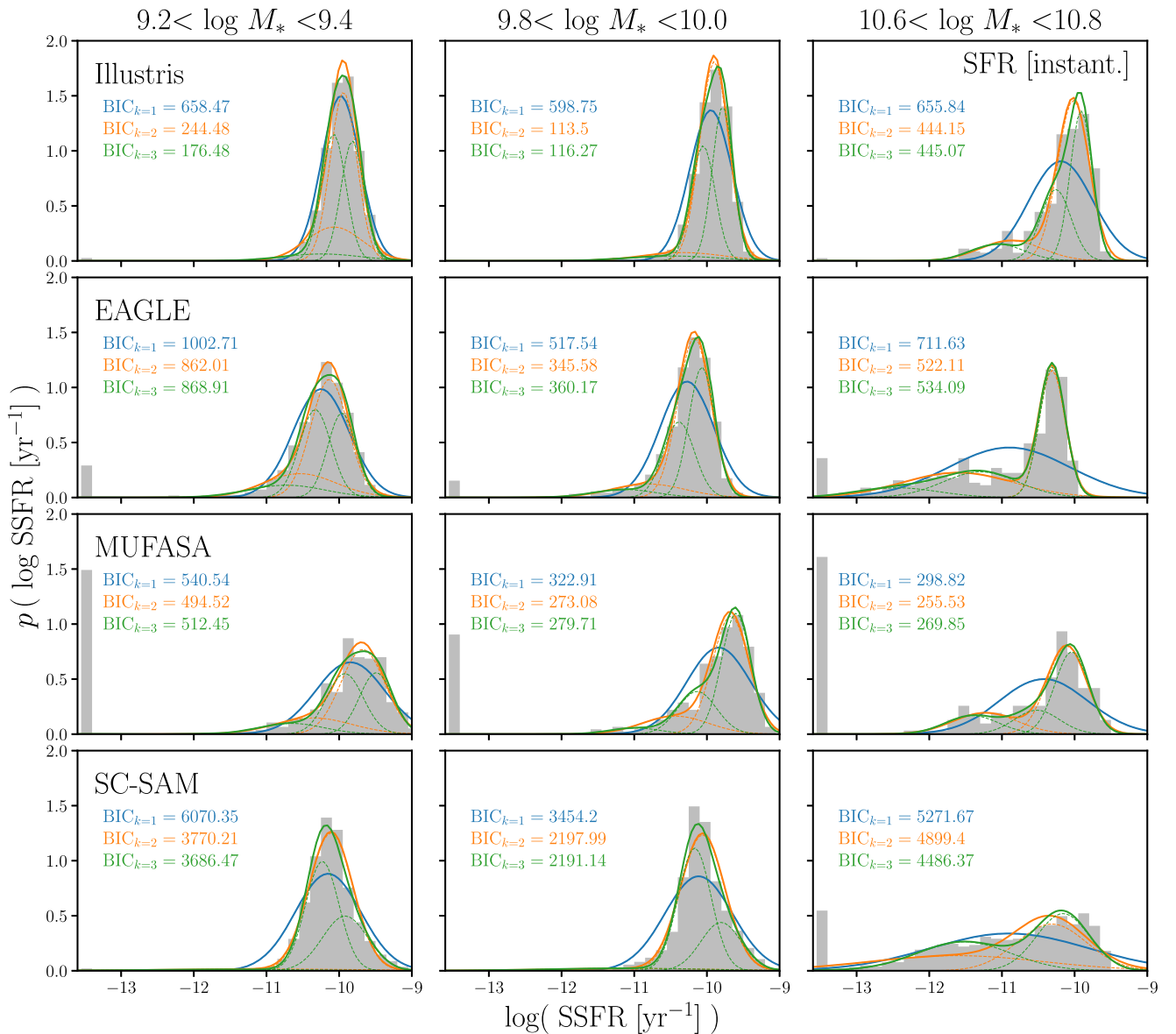
Figure 11. GMMs with $k = 1$, 2, and 3 (blue, orange, and green) components fit to the instantaneous SSFR distributions, $P(\log \text{SSFR})$, of the Illustris, EAGLE, MUFASA, and SC-SAM (top to bottom panels) centrals in three stellar mass bins: [9.2, 9.4], [9.8, 10.], and [10.6, 10.8] (left to right). We represent galaxies with unmeasurably low SFR in $P(\log \text{SSFR})$s with $\log \text{SSFR} = -13.5$. For every GMM fit, we plot each component in dash lines and list their BICs in the same color. In our SFS fitting, we select the GMM with the lowest BIC as the best fit. This provides a data-driven way of accurately fitting the SSFR distribution while avoiding overfitting.

find discrepancies in the SFSs on the order of ∼0.5 dex (center and right panels of 10). This illustrates that the agreement found in Somerville & Davé (2015) is driven in large part by the difference in methods used to measure SFSs. Furthermore, the difference between the Illustris and MUFASA SFSs in the panels illustrates how different SFS fitting methods, even when consistently applied, can alter the difference between SFSs. The difference between the Illustris and MUFASA SFSs is significantly larger in the center panel when the $\text{SSFR} > 10^{-11} \, \text{yr}^{-1}$ cut is applied and galaxies with SFR below the resolution limit, which make up a larger fraction of the MUFASA galaxies than the Illustris galaxies, are removed by the selection cut. In the center panel of Figure 10, we find consistency among the slopes of the different SFSs. This consistency is a result of the hard selection cut, which biases the SFS slopes closer to the cut ($\text{SSFR} = 10^{-11} \, \text{yr}^{-1}$) and thus to one another. These effects highlight the impact of hard selection scuts and the need for a consistent data-driven method for

identifying the SFS that better account for intrinsically different SFR–M_* distributions in the simulations.

Appendix B
Identifying the SFS Using Gaussian Mixture Models

In order to derive the best-fit GMM used for identifying the SFS in each M_* bin, we compare GMM fits with $k \leqslant 3$ components using their BICs (Section 3). In Figures 11 and 12, we illustrate this comparison among the GMMs with $k = 1$, 2, and 3 (blue, orange, and green) components fit to the instantaneous SSFR distributions, $P(\log \text{SSFR})$, of the Illustris, EAGLE, MUFASA, and SC-SAM (top to bottom panels) centrals in three stellar mass bins: $9.2 < \log M_* < 9.4$, $9.8 < \log M_* < 10$, and $10.6 < \log M_* < 10.8$ (left to right). The SSFR distributions in Figures 11 and 12 are derived using instantaneous and 100 Myr SFRs respectively. Galaxies with
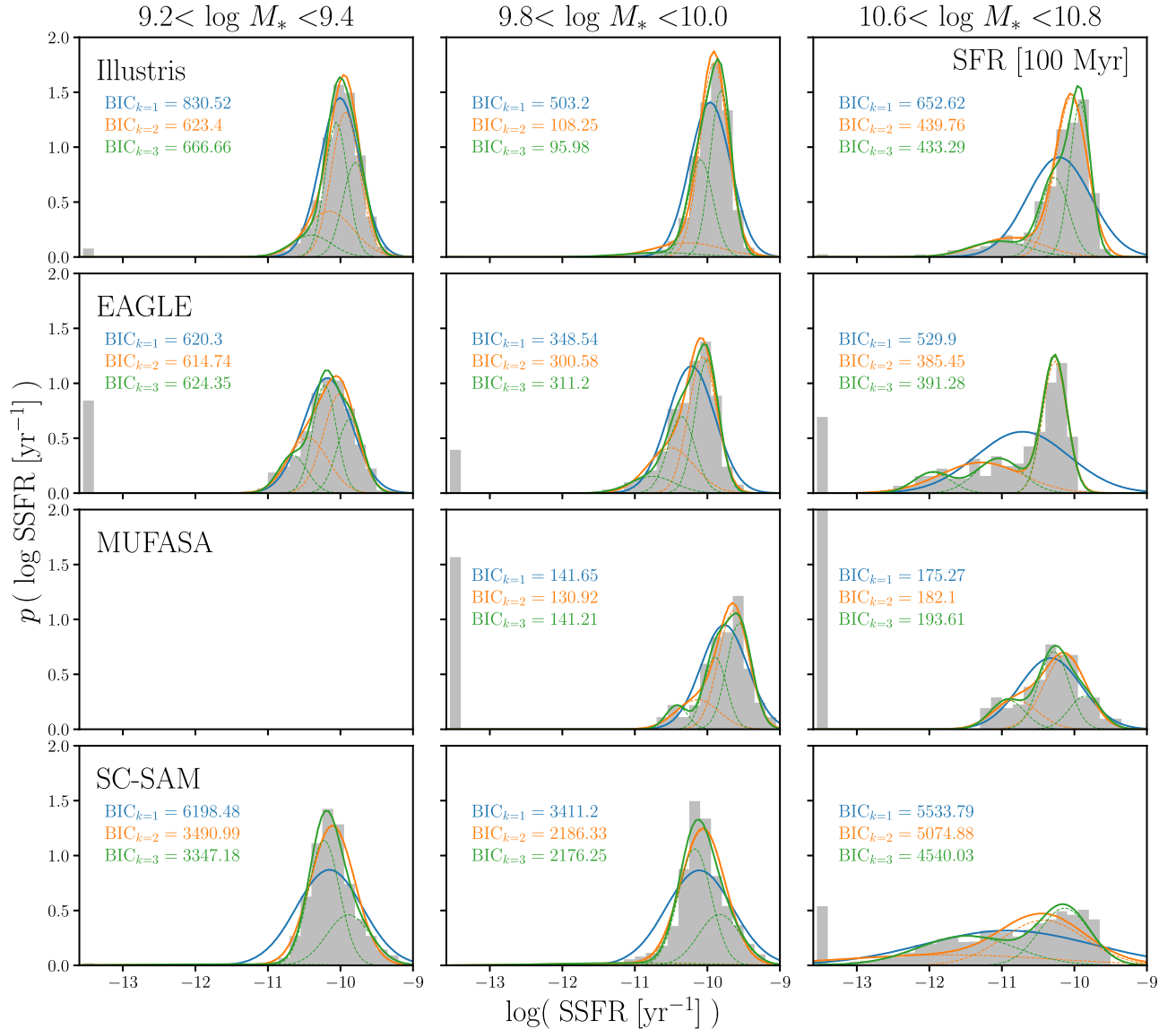
Figure 12. Same as Figure 11 but for the 100 Myr SSFR distributions.

unmeasurably low SFR are represented at the edge of the SSFR distributions with log SFR $= -13.5$. In each panel, we also present the BICs and plot every component of the GMM fits (dashed) in their respective colors. These figures illustrate the advantages of the data-driven GMM based fitting and BIC based model selection used in our SFS fitting.

For instance, in most of the highest M_* bin (right panels in both figures) the $k = 1$ GMM fits do not reflect the clearly bimodal SSFR distributions. In these cases, the $BIC_{k=1}$ is significantly larger than $BIC_{k=2}$ and $BIC_{k=3}$, so our BIC based model selection favors GMMs with more than one component. In fact, GMMs with more components are more flexible and generally can better fit the underlying distribution. However as the EAGLE and MUFASA $9.8 < \log M_* < 10$ bins of the figures illustrate, our BIC based model selection does not always favor the higher k GMM fits. Although the $k = 3$ GMMs have the lowest χ^2 in these panels, because of the penalty term for the number of model parameters, our BIC criteria favors the $k = 2$ GMMs. According to the BICs, the $k = 3$ GMMs in these panels overfit the SSFR distributions. The figures also illustrate that among the GMM fits with comparably low BICs,

the dominant component that describe the star-forming portion of $P(\log SSFR)$ is not significantly impacted. Since this component is mainly identified as the SFS, our BIC based model selection does not strongly impact the position and width of the SFS.

From the best-fit GMMs, we identify the SFS components iteratively starting from the lowest M_* bin as described in Section 3.1. We consider other components, depending on their mean, as low, intermediate, or high SF components in Section 4.2. The SC-SAM in particular has high SF components at $M_* \lesssim 10^{10} M_\odot$ (bottom left and center panels of Figures 11 and 12). In these cases, the SSFR distribution is not well described by a single log-normal distribution. Instead the distribution is significantly asymmetric with a heavier tail on the more star-forming end of the distribution. An extra component to account for the non-Gaussianity improves the fit more than the penalty term, giving us the high SF components. Our method for identifying the SFS and other components using GMMs assumes that the components are Gaussian. However, from the data alone, it is impossible to determine the shape of the "true" galaxy subpopulation distributions. While mixture models with non-Gaussian components can be used instead, without
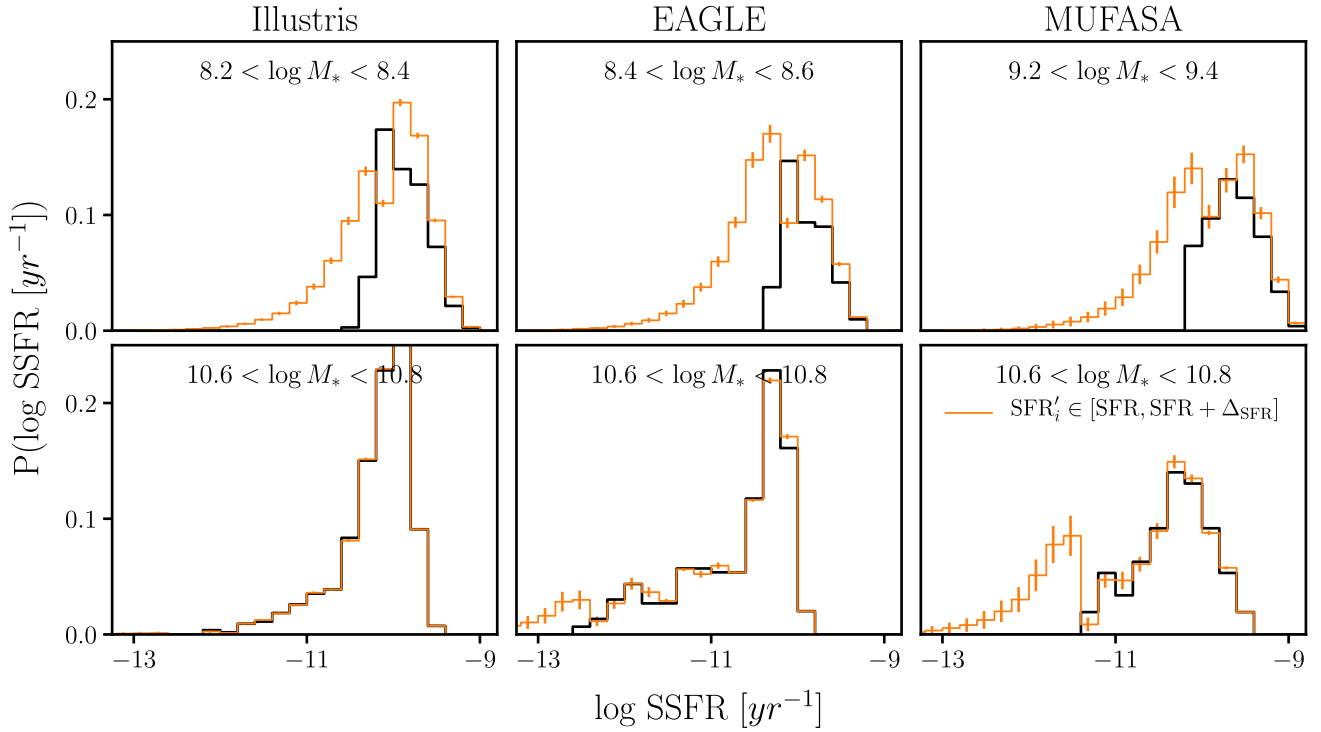
Figure 13. Impact of SFR resolution on the SSFR distribution, $P(\log \mathrm{SSFR})$, in two stellar mass bins of the hydrodynamic simulations: Illustris (left), EAGLE (center), and MUFASA (right). We plot the $P(\mathrm{SSFR})$ distributions using the 100 Myr SFRs with resolution effects in black. These exclude galaxies with unmeasurably low SFRs. In orange, we plot the $P(\log \mathrm{SSFR})$ distributions where the SFRs of the galaxies are sampled uniformly within the SFR resolution range ($[\mathrm{SFR}_i, \mathrm{SFR}_i + \Delta_{\mathrm{SFR}}]$). The uncertainties for the orange $P(\mathrm{SSFR})$s are estimated from resampling the SFR of each galaxy based on the SFR resolution. At low stellar masses (top) the SFR resolution significantly impacts the star-forming end of $P(\mathrm{SSFR})$s. At higher stellar masses, although the SFR resolution impacts the $P(\mathrm{SSFR})$s, the effect is limited to below $\log \mathrm{SSFR} < -11$.
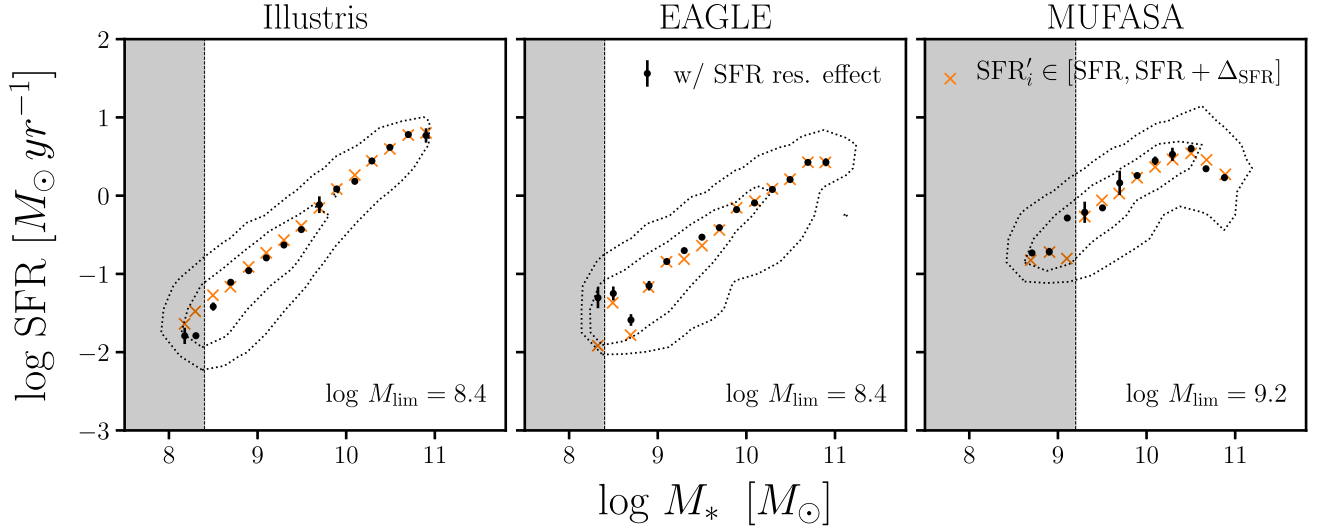

Figure 14. Resolution effect of 100 Myr SFRs in the hydrodynamic simulations (Illustris, EAGLE, and MUFASA) impact the identified SFSs at low stellar masses. In black we plot the best-fit SFS with the resolution effects. In orange we plot the best-fit SFS where the SFR for each galaxy is sampled uniformly within the resolution range: $\mathrm{SFR}'_i \in [\mathrm{SFR}_i, \mathrm{SFR}_i + \Delta_{\mathrm{SFR}}]$). Based on the discrepancy between the fits, we determine stellar mass limits above which the SFR resolution does not significantly impact (<0.2 dex) the identified SFS. For Illustris, EAGLE, and MUFASA this corresponds to $\log M_{\mathrm{lim}} = 8.4$, 8.4, and 9.2, as shown in the gray shaded region.

knowing the "true" subpopulations, they will still require assumptions on the shape of the components. Therefore, in Section 4.2 when we discuss components besides the SFS (low, intermediate, and high), we distinguish between the components and the galaxy subpopulations commonly referred to in the literature (quiescent, transitioning, and starburst).

Appendix C
Resolution Effects in Hydrodynamic Simulations

In our analysis, we consistently derive SFRs for all of the simulated galaxies on two timescales: instantaneous and averaged over 100 Myr (Section 2). For the hydrodynamic simulations, an SFR averaged over 100 Myr is derived using
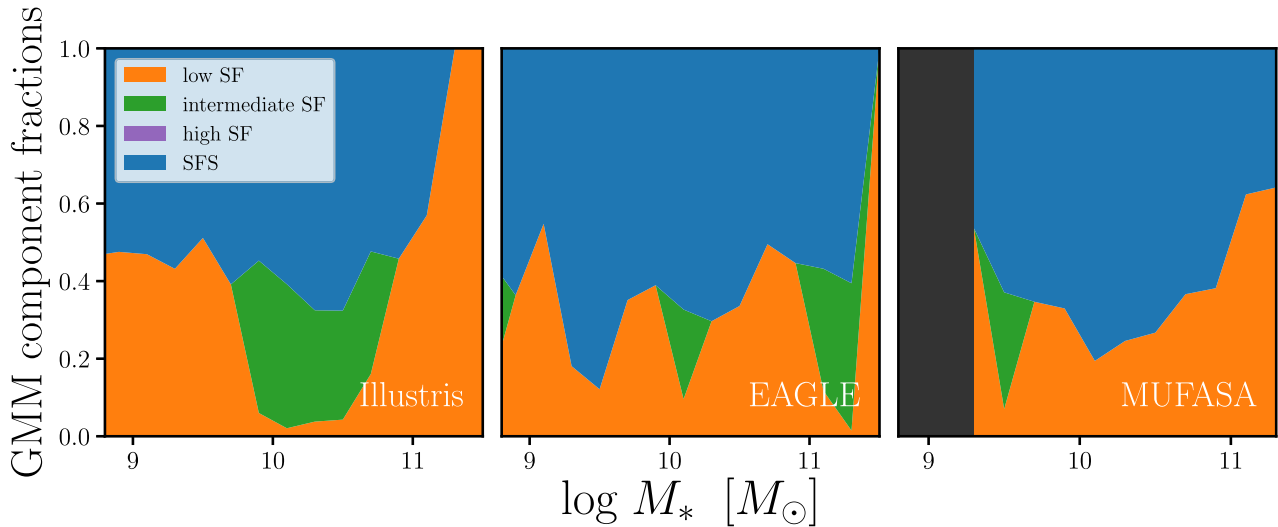
Figure 15. Fractional contributions, π_i, of the best-fit GMM components from our method for the hydrodynamic simulations (Illustris, EAGLE, and MUFASA) where we uniformly sample the 100 Myr SFRs within the SFR resolution range—$\mathrm{SFR}_i' \in [\mathrm{SFR}_i, \mathrm{SFR}_i + \Delta_{\mathrm{SFR}}]$. Compared to Figure 9, we find SFR resolution has no significant impact on the qualitative results in Section 4.2.

the formation times of the star particles in the simulation, which means that the mass and temporal resolutions of the simulations impact the 100 Myr SFR. In Illustris, EAGLE, and MUFASA, their 100 Myr SFRs have resolutions of $\Delta_{\mathrm{SFR}} = 0.0126, 0.018$, and $0.182\ M_\odot\ \mathrm{yr}^{-1}$, corresponding to baryon particle masses of $1.26 \times 10^6\ M_\odot$, $1.8 \times 10^6\ M_\odot$, and $1.82 \times 10^7\ M_\odot$, respectively. For SFR averaged over 10 Myr, the Δ_{SFR}s would be 10 times larger. Therefore, we instead use instantaneous SFRs to measure star formation on the shortest timescale.

For galaxies with high 100 Myr SFR, the resolution Δ_{SFR} is relatively small compared to their SFRs and therefore it does not have a significant impact. However, for low SFR galaxies, the resolution effect is more significant. At the lowest SFR end, galaxies that, without the resolution effect would have SFRs in the range of $0 < \mathrm{SFR} < \Delta_{\mathrm{SFR}}$, may have unmeasurably low SFR ($\mathrm{SFR} = 0$) with the resolution effect. These galaxies are thereby not included in the SFR–M_* plane or when we identify the SFS. In Figure 13, we present the impact of excluding these galaxies and the overall resolution effect on the $P(\log \mathrm{SSFR})$ distributions of the hydrodynamic simulations in two stellar mass bins. In black, we plot the $P(\log \mathrm{SSFR})$ distributions using the 100 Myr SFRs with resolution effects (excluding galaxies with unmeasurably low SFR). In orange, we plot the $P(\log \mathrm{SSFR})$ distributions of *all* galaxies where SFR_i' of each galaxy sampled uniformly within the SFR resolution range $[\mathrm{SFR}_i, \mathrm{SFR}_i + \Delta_{\mathrm{SFR}}]$. Uncertainties for the orange P $(\log \mathrm{SSFR})$s are derived from repeating this SFR sampling 100 times. For the low M_* bins (top), the SFR resolution affects the $P(\log \mathrm{SSFR})$s well above $\log \mathrm{SSFR} = -11.0$ on the star-forming end of the distribution. Meanwhile, the impact at higher M_* (bottom), is limited to the low SSFR end.

In order to better quantify the impact of the SFR resolution effect on our SFS fitting, in Figure 14 we compare the SFS fits using 100 Myr SFRs *with* resolution effects (black) to the SFS fits using 100 Myr SFRs sampled uniformly within the SFR resolution range (orange; $\mathrm{SFR}_i' \in [\mathrm{SFR}_i, \mathrm{SFR}_i + \Delta_{\mathrm{SFR}}]$). The uncertainties of our SFS fits in black are calculated using bootstrap resampling (Section 3). In agreement with Figure 13, we find that the SFR resolution significantly impacts the identified SFS at low M_*. Moreover, using the comparison of

Figure 14, we determine the stellar mass limit above which the SFR resolution does not significantly impact the identified SFS—i.e., the shift in best-fit SFS is below 0.2 dex. For Illustris, EAGLE, and MUFASA we determine $\log M_{\mathrm{lim}} = 8.4, 8.4$, and 9.2, respectively. For EAGLE, where we have a higher resolution box ($8\times$ higher baryon mass resolution) available, we further confirm that the SFS is not significantly impacted above $\log M_{\mathrm{lim}}$.

In addition to its effect on the SFS fits, we also examine the impact of SFR resolution on our results regarding the non-SFS components of our GMM fitting (Figure 9). In Figure 15 we present the fraction contributions (π_i) of the best-fit components for the Illustris, EAGLE, and MUFASA simulations, where we uniformly sample the SFRs within the SFR resolution range (same as above). Besides no longer having a component of galaxies with unmeasurably low SFRs due to the SFR sampling, we find no significant change from the π_i of Figure 9 and, thus, the results of Section 4.2.

In addition to its impact on the SFRs, the mass resolution of the hydrodynamic simulations also impacts the stellar masses of the simulations. We note that the SMFs differ with resolution as shown in Schaye et al. (2015), Genel et al. (2014), and Davé et al. (2016). To determine whether mass resolution has a significant impact on the identified SFS, we compare the SFS identified from our EAGLE simulation (Section 2) to SFS identified from the higher mass resolution L0025N0752 EAGLE simulation (Schaye et al. 2015). The L0025N0752 simulation has a baryonic mass resolution of $2.26 \times 10^5\ M_\odot$ ($8\times$ higher than our EAGLE simulation). From the comparison, we find that the SFS is underestimated near the mass resolution in our lower resolution EAGLE simulation. However, this impacts the SFS by less than 0.2 dex. Although higher resolution simulations for Illustris are not available, we also compare the SFS identified from our Illustris simulations with SFSs identified from lower resolution Illustris simulations ($8\times$ and $64\times$ lower resolutions) and find qualitatively consistent results. Therefore, we find that the effect of mass resolution on the stellar masses in hydrodynamic simulations does not significantly impact the SFS identified in the

simulations, especially above the stellar mass limits of our analysis.

ORCID iDs

Tjitske K. Starkenburg ● https://orcid.org/0000-0003-2539-8206
Ena Choi ● https://orcid.org/0000-0002-8131-6378
Marla C. Geha ● https://orcid.org/0000-0002-7007-9725
Shy Genel ● https://orcid.org/0000-0002-3185-1540
Christopher C. Hayward ● https://orcid.org/0000-0003-4073-3236
Ariyeh H. Maller ● https://orcid.org/0000-0003-2060-8331
Viraj Pandya ● https://orcid.org/0000-0002-2499-9205
Gergö Popping ● https://orcid.org/0000-0003-1151-4659

References

Abazajian, K. N., Adelman-McCarthy, J. K., Agüeros, M. A., et al. 2009, ApJS, 182, 543
Abramson, L. E., Gladders, M. D., Dressler, A., et al. 2016, ApJ, 832, 7
Aihara, H., Allende Prieto, C., An, D., et al. 2011, ApJS, 193, 29
Arthur, D., & Vassilvitskii, S. 2007, in Proc. Eighteenth Annual ACM-SIAM Symp. Discrete Algorithms 2007 (Philadelphia, PA: Society for Industrial and Applied Mathematics), 1027
Astropy Collaboration, Robitaille, T. P., Tollerud, E. J., et al. 2013, A&A, 558, 33
Baldry, I. K., Balogh, M. L., Bower, R. G., et al. 2006, MNRAS, 373, 469
Balogh, M. L., Schade, D., Morris, S. L., et al. 1998, ApJL, 504, L75
Behroozi, P. S., Wechsler, R. H., & Conroy, C. 2013a, ApJ, 770, 57
Behroozi, P. S., Wechsler, R. H., & Wu, H.-Y. 2013b, ApJ, 762, 109
Bigiel, F., Leroy, A., Walter, F., et al. 2008, AJ, 136, 2846
Bisigello, L., Caputi, K. I., Grogin, N., & Koekemoer, A. 2018, A&A, 609, A82
Blanton, M. R. 2006, ApJ, 648, 268
Blanton, M. R., Hogg, D. W., Bahcall, N. A., et al. 2003, ApJ, 594, 186
Blanton, M. R., Kazin, E., Muna, D., Weaver, B. A., & Price-Whelan, A. 2011, AJ, 142, 31
Blanton, M. R., & Moustakas, J. 2009, ARA&A, 47, 159
Blanton, M. R., & Roweis, S. 2007, AJ, 133, 734
Blanton, M. R., Schlegel, D. J., Strauss, M. A., et al. 2005, AJ, 129, 2562
Bluck, A. F. L., Mendel, J. T., Ellison, S. L., et al. 2016, MNRAS, 462, 2559
Borch, A., Meisenheimer, K., Bell, E. F., et al. 2006, A&A, 453, 869
Bovy, J., Hogg, D. W., & Roweis, S. T. 2011, AnApS, 5, 1657
Brennan, R., Pandya, V., Somerville, R. S., et al. 2015, MNRAS, 451, 2933
Brennan, R., Pandya, V., Somerville, R. S., et al. 2017, MNRAS, 465, 619
Brinchmann, J., Charlot, S., White, S. D. M., et al. 2004, MNRAS, 351, 1151
Broderick, A. E., Fish, V. L., Doeleman, S. S., & Loeb, A. 2011, ApJ, 735, 110
Bruzual, A. G., & Charlot, S. 1993, ApJ, 405, 538
Bundy, K., Ellis, R. S., Conselice, C. J., et al. 2006, ApJ, 651, 120
Chabrier, G. 2003, PASP, 115, 763
Charlot, S., & Fall, S. M. 2000, ApJ, 539, 718
Collaboration, T. A., Price-Whelan, A. M., Sipőcz, B. M., et al. 2018, AJ, 156, 123
Crain, R. A., Schaye, J., Bower, R. G., et al. 2015, MNRAS, 450, 1937
Daddi, E., Dickinson, M., Morrison, G., et al. 2007, ApJ, 670, 156
Dalla Vecchia, C., & Schaye, J. 2012, MNRAS, 426, 140
Davé, R., Rafieferantsoa, M. H., & Thompson, R. J. 2017a, arXiv:1704.01135
Davé, R., Rafieferantsoa, M. H., Thompson, R. J., & Hopkins, P. F. 2017b, MNRAS, 467, 115
Davé, R., Thompson, R., & Hopkins, P. F. 2016, MNRAS, 462, 3265
Davis, M., Efstathiou, G., Frenk, C. S., & White, S. D. M. 1985, ApJ, 292, 371
Dempster, A. P., Laird, N. M., & Rubin, D. B. 1977, Journal of the Royal Statistical Society. Series B (Methodological), 39, 1
Efron, B. 1979, AnSta, 7, 1
Feldmann, R. 2017, MNRAS, 470, L59
Ferland, G. J. 1996, Hazy, A Brief Introduction to Cloudy 90 (Lexington, KY: Univ. Kentucky)
Fraley, C., & Raftery, A. E. 1998, CompJ, 41, 578
Furlong, M., Bower, R. G., Theuns, T., et al. 2015, MNRAS, 450, 4486
Gabor, J. M., & Davé, R. 2015, MNRAS, 447, 374
Geha, M., Blanton, M. R., Yan, R., & Tinker, J. L. 2012, ApJ, 757, 85
Genel, S., Bryan, G. L., Springel, V., et al. 2018, arXiv:1807.07084

Genel, S., Vogelsberger, M., Springel, V., et al. 2014, MNRAS, 445, 175
Gill, S. P. D., Knebe, A., & Gibson, B. K. 2005, MNRAS, 356, 1327
Gnedin, N. Y., & Kravtsov, A. V. 2011, ApJ, 728, 88
Hahn, C., Blanton, M. R., Moustakas, J., et al. 2015, ApJ, 806, 162
Hahn, C., Tinker, J. L., & Wetzel, A. R. 2017, ApJ, 841, 6
Hao, J., Koester, B. P., Mckay, T. A., et al. 2009, ApJ, 702, 745
Hopkins, A. M., & Beacom, J. F. 2006, ApJ, 651, 142
Hopkins, P. F. 2015, MNRAS, 450, 53
Hunter, J. D. 2007, CSE, 9, 90
Iovino, A., Cucciati, O., Scodeggio, M., et al. 2010, A&A, 509, A40
Jones, E., Oliphant, E., Peterson, P., et al. 2001, SciPy: Open Source Scientific Tools for Python, http://www.scipy.org/
Kauffmann, G., Heckman, T. M., White, S. D. M., et al. 2003, MNRAS, 341, 54
Kelson, D. D. 2014, arXiv:1406.5191
Kennicutt, R. C., & Evans, N. J. 2012, ARA&A, 50, 531
Krumholz, M. R., & Gnedin, N. Y. 2011, ApJ, 729, 36
Lee, K. J., Guillemot, L., Yue, Y. L., Kramer, M., & Champion, D. J. 2012, MNRAS, 424, 2832
Lee, N., Sanders, D. B., Casey, C. M., et al. 2015, ApJ, 801, 80
Leja, J., van Dokkum, P. G., Franx, M., & Whitaker, K. E. 2015, ApJ, 798, 115
Leroux, B. G. 1992, AnSta, 20, 1350
Liddle, A. R. 2007, MNRAS, 377, L74
Lloyd, S. 1982, ITIT, 28, 129
Madau, P., & Dickinson, M. 2014, ARA&A, 52, 415
Magdis, G. E., Daddi, E., Béthermin, M., et al. 2012, ApJ, 760, 6
Mamon, G. A., Sanchis, T., Salvador-Solé, E., & Solanes, J. M. 2004, A&A, 414, 445
McAlpine, S., Helly, J. C., Schaller, M., et al. 2016, A&C, 15, 72
McLachlan, G., & Peel, D. 2000, Finite Mixture Models (New York: Wiley-Interscience)
Mitra, S., Davé, R., & Finlator, K. 2015, MNRAS, 452, 1184
Moustakas, J., Coil, A. L., Aird, J., et al. 2013, ApJ, 767, 50
Muratov, A. L., Kereš, D., Faucher-Giguère, C.-A., et al. 2015, MNRAS, 454, 2691
Neal, R. M., & Hinton, G. E. 1998, in Learning in Graphical Models (Dordrecht: Springer), 355
Nelson, D., Pillepich, A., Genel, S., et al. 2015, A&C, 13, 12
Noeske, K. G., Weiner, B. J., Faber, S. M., et al. 2007, ApJL, 660, L43
Oppenheimer, B. D., & Davé, R. 2006, MNRAS, 373, 1265
Pandya, V., Brennan, R., Somerville, R. S., et al. 2017, MNRAS, 472, 2054
Pedregosa, F., Varoquaux, G., Gramfort, A., et al. 2011, Journal of Machine Learning Research, 12, 2825
Peng, Y.-j., Lilly, S. J., Kovač, K., et al. 2010, ApJ, 721, 193
Popping, G., Somerville, R. S., & Trager, S. C. 2014, MNRAS, 442, 2398
Porter, L. A., Somerville, R. S., Primack, J. R., & Johansson, P. H. 2014, MNRAS, 444, 942
Press, W. H., Teukolsky, S. A., Vetterling, W. T., & Flannery, B. P. 1992, Numerical Recipes in C: The Art of Scientific Computing (New York: Cambridge Univ. Press)
Rodríguez-Puebla, A., Behroozi, P., Primack, J., et al. 2016, MNRAS, 462, 893
Roeder, K., & Wasserman, L. 1997, J. Am. Stat. Assoc., 92, 894
Salim, S., Rich, R. M., Charlot, S., et al. 2007, ApJS, 173, 267
Schaller, M., Dalla Vecchia, C., Schaye, J., et al. 2015, MNRAS, 454, 2277
Schaye, J., Crain, R. A., Bower, R. G., et al. 2015, MNRAS, 446, 521
Schreiber, C., Pannella, M., Elbaz, D., et al. 2015, A&A, 575, A74
Schwarz, G. 1978, AnSta, 6, 461
Sijacki, D., Springel, V., Di Matteo, T., & Hernquist, L. 2007, MNRAS, 380, 877
Somerville, R. S., Barden, M., Rix, H.-W., et al. 2008a, ApJ, 672, 776
Somerville, R. S., & Davé, R. 2015, ARA&A, 53, 51
Somerville, R. S., Gilmore, R. C., Primack, J. R., & Domínguez, A. 2012, MNRAS, 423, 1992
Somerville, R. S., Hopkins, P. F., Cox, T. J., Robertson, B. E., & Hernquist, L. 2008b, MNRAS, 391, 481
Somerville, R. S., Popping, G., & Trager, S. C. 2015, MNRAS, 453, 4337
Somerville, R. S., & Primack, J. R. 1999, MNRAS, 310, 1087
Somerville, R. S., Primack, J. R., & Faber, S. M. 2001, MNRAS, 320, 504
Sparre, M., Hayward, C. C., Springel, V., et al. 2015, MNRAS, 447, 3548
Sparre, M., & Springel, V. 2017, MNRAS, 470, 3946
Speagle, J. S., Steinhardt, C. L., Capak, P. L., & Silverman, J. D. 2014, ApJS, 214, 15
Springel, V. 2005, MNRAS, 364, 1105
Springel, V. 2010, MNRAS, 401, 791
Springel, V., & Hernquist, L. 2003, MNRAS, 339, 289

Springel, V., White, S. D. M., Tormen, G., & Kauffmann, G. 2001, MNRAS, 328, 726

Steele, R. J., & Raftery, A. E. 2010, in Frontiers of Statistical Decision Making and Bayesian Analysis, ed. M.-H. Chen et al. (Berlin: Springer), 13

Taylor, E. N., Franx, M., van Dokkum, P. G., et al. 2009, ApJ, 694, 1171

Taylor, E. N., Hopkins, A. M., Baldry, I. K., et al. 2015, MNRAS, 446, 2144

Terrazas, B. A., Bell, E. F., Woo, J., & Henriques, B. M. B. 2017, ApJ, 844, 170

Tinker, J., Wetzel, A., & Conroy, C. 2011, arXiv:1107.5046

Torrey, P., Vogelsberger, M., Genel, S., et al. 2014, MNRAS, 438, 1985

Trayford, J. W., Camps, P., Theuns, T., et al. 2017, MNRAS, 470, 771

Trayford, J. W., Theuns, T., Bower, R. G., et al. 2015, MNRAS, 452, 2879

Vakili, M., & Hahn, C. H. 2016, arXiv:1610.01991

Vanderplas, J., Connolly, A., Ivezi'c, Z., & Gray, A. 2012, in Proc. Conf. on Intelligent Data Understanding (CIDU) (Piscataway, NJ: IEEE), 47

Van Der Walt, S., Colbert, S. C., & Varoquaux, G. 2011, arXiv:1102.1523

Vogelsberger, M., Genel, S., Sijacki, D., et al. 2013, MNRAS, 436, 3031

Vogelsberger, M., Genel, S., Springel, V., et al. 2014, MNRAS, 444, 1518

Wang, H., Mo, H. J., & Jing, Y. P. 2009, MNRAS, 396, 2249

Wang, L., Farrah, D., Oliver, S. J., et al. 2013, MNRAS, 431, 648

Wang, L., Norberg, P., Brough, S., et al. 2018, arXiv:1802.08456

Wetzel, A. R., Tinker, J. L., & Conroy, C. 2012, MNRAS, 424, 232

Wetzel, A. R., Tinker, J. L., Conroy, C., & van den Bosch, F. C. 2013, MNRAS, 432, 336

Wetzel, A. R., Tinker, J. L., Conroy, C., & van den Bosch, F. C. 2014, MNRAS, 439, 2687

Whitaker, K. E., van Dokkum, P. G., Brammer, G., & Franx, M. 2012, ApJL, 754, L29

Yan, R. 2011, AJ, 142, 153

Yan, R., & Blanton, M. R. 2012, ApJ, 747, 61

York, D. G., Adelman, J., Anderson, J. E., Jr., et al. 2000, AJ, 120, 1579